



Review article

Challenges and recent progress in fast-charging lithium-ion battery materials



Jianhui He^a, Jingke Meng^a, Yunhui Huang^{a,b,*}

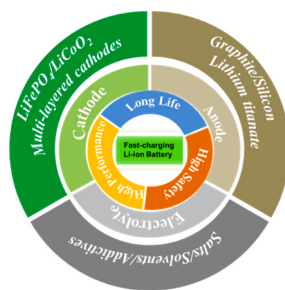
^a Institute of New Energy Vehicles, School of Materials Science and Engineering, Tongji University, Shanghai, 201804, PR China

^b State Key Laboratory of Material Processing and Die & Mould Technology, School of Materials Science and Engineering, Huazhong University of Science and Technology, Wuhan, 430074, PR China

HIGHLIGHTS

- The progress of fast-charging electrode materials for lithium-ion batteries is reviewed.
- The critical factors for designing fast-charging electrode materials are discussed.
- The optimization strategies of fast-charging electrode materials are proposed.

GRAPHICAL ABSTRACT



ARTICLE INFO

Keywords:

Lithium-ion batteries
Fast charging materials
Lithium diffusion
Mass transport
Electrochemical performance

ABSTRACT

Fast charging of lithium-ion batteries (LIBs) is one of the key factors to limit the widespread application of electric vehicles, especially when compared to the rapid refueling of conventional internal combustion engine vehicles. The electrode materials are most critical for fast charging, which performances under high-rate condition greatly affect the fast-charging capability of the batteries. This review summarizes the current progress of research and development in anode, cathode and electrolyte materials for fast-charging LIBs. On understanding the intrinsic structures and lithium storage mechanisms of the active materials, key challenges and strategies to achieve fast-charging capabilities are discussed, and the perspectives are presented.

1. Introduction

With the widespread application of electrochemical energy storage in portable electronics and electric vehicles (EVs), the requirements and reliance on lithium-ion batteries (LIBs) become higher than ever [1–3]. After decades of development, a major challenge to the widespread application of EVs is "range anxiety" compared to conventional internal combustion engine vehicles. Using fast charging stations can help to

address the range concerns of consumers. Currently, Tesla, the global leader in the EV industry, uses a third-generation charging stations (250 kW), which can travel about 250 km in 15 min, but it still cannot meet the fast-charging requirement. In order to provide refueling times comparable to conventional combustion engine vehicles, a range of 400 km is usually required in 15 min. However, ultrafast charging brings new challenges for battery materials that need to be further addressed.

Currently, the battery materials used in EVs are mainly graphite,

* Corresponding author. Institute of New Energy Vehicles, School of Materials Science and Engineering, Tongji University, Shanghai, 201804, PR China.
E-mail address: huangyh@mail.hust.edu.cn (Y. Huang).

lithium titanate or silicon-based anode materials, lithium iron phosphate (LiFePO_4) or ternary layered cathode materials, and non-aqueous electrolytes. The electrode polarization is the main reason for battery failure to affect fast charging. The factors mainly include the diffusion rate of Li^+ ions in the active materials, the transport of Li^+ ions in the electrolyte, and the charge transfer kinetics at the electrode/electrolyte interface. From the view of electrode materials, Li plating at anode side and Li^+ ions diffusion in the cathode are primarily rate-limiting. Commonly-used graphite anode usually exhibits poor kinetics and low working potential (0.1 V vs. Li/Li^+) at high charge rates ($> 1 \text{ C}$), serious problems such as mechanical cracks, interfacial side reaction, and anodic polarization, result in Li plating and heat generation, leading to performance degradation and safety concern [4]. As the charging process continues, the vacancies in the graphite layer decrease, so the intercalation current decreases, and the lithium plating current increases, which greatly reduces the battery life and limits the fast-charging capability [5]. Therefore, fast-charging anode materials must be constructed to accelerate the kinetics of Li^+ intercalation and reduce the overpotential, thereby keeping the anode potential away from unwanted Li plating (0 V vs. Li/Li^+) [6,7]. For cathode materials, the larger volume change, increased heterogeneity and the resulting microcracks at high Li insertion rates than low rates can increase interfacial side reactions [8]. During the fast-charging process, the migration rate of Li^+ ions and the electrochemical reduction of the electrolyte at the electrode interface further lead to a decrease in capacity, an increase in potential polarization, and potential safety hazards. Usually, the typical resolution strategies include the introduction of suitable electrolytes with high ionic conductivity, weak solvation, and construction of stable solid electrolyte interphase (SEI)/cathode electrolyte interphase (CEI) film [9,10].

In this review, we summarize the current status of fast-charging anode and cathode materials for rechargeable batteries, introduce the key factors to influence the fast-charging performance, and provide a guidance for the design of fast charging LIBs. Challenges in practical applications and current strategies to improve the electrochemical performance of electrode materials are also discussed. In addition, the commercially-used LiPF_6 -carbonate-based electrolytes also affect battery performance and lifetime during fast charging. Design aspects of fast-charging electrolytes are therefore discussed and proposed. By understanding the natures of the electrode materials, we provide a guidance for designing LIBs with excellent rate performance.

2. Requirements of fast-charging materials

Fast-charging batteries are usually developed by improving the rate capability of conventional rechargeable batteries at high current densities. In order to develop fast charging materials, it is necessary to understand the working principle of the battery and the electrochemical reaction rate control steps to improve the kinetic performance. During the charging process, Li^+ ions are first extracted from the cathode material and then diffuse into the liquid electrolyte through the cathode/electrolyte interface; the extracted Li^+ ions are subsequently solvated by solvent molecules; the solvated Li^+ ions migrate through the separator to the anode side, and then are desolvated at anode/electrolyte interface; finally the desolvated Li^+ ions are inserted into the interior of the anode material. At the same time, the electrons generated by the cathode are transferred to the current collector, and then move to the anode through the external circuit. In order to achieve fast charging, low energetic barriers are required for Li-ion migration into and Li-ion diffusion inside the active materials. The resistance of battery can be used to judge the energetic barriers. AC impedance spectroscopy is employed to analyze the resistance, including bulk resistance (electronic conductivity of materials, R_Ω), interface resistance (ohmic resistance of solid electrolyte interphase (SEI), R_{SEI}), charge transfer resistance (kinetics of electrode reactions, R_{ct}), Warburg impedance (diffusion of Li^+ ions, W) through equivalent circuits, which reflect the corresponding activation energy of

each step (Fig. 1). The rate capability of LIBs mainly depends on the mobility of ions and electrons within the composite electrodes and their interfaces, as well as the electrolyte. Fast charging requires high current density. Poor ion and electron transport kinetics of the active materials create high overpotentials, which can cause side physicochemical reaction and lead to battery failure. Therefore, the fast-charging active materials require three basic features: high Li^+ ions diffusion coefficient, excellent charge transfer kinetic performance, and controllable Li^+ ions transport.

Understanding the electron conduction mechanism and constructing the electrodes with excellent electrical conductivity can facilitate fast battery charging. According to the energy band theory, electrons in the valence band pass through the forbidden band into the conduction band, thereby enabling the electrode materials to conduct electricity. According to the definition of the electron conduction properties in materials, the electron mobility σ can be expressed by $\sigma = n|e|\mu_e$, where n is the number of carriers, $|e|$ is the absolute value of the charge carried by carriers, and μ_e is the mobility of carriers. Considering the existence of free electrons and holes in the materials, the relationship between conductivity and carrier mobility can be further described as $\sigma = n_i e \mu_e + m_i e \mu_h$, where n_i and μ_e represent the concentrations and mobility of electrons, respectively, and m_i and μ_h are the concentration and mobility of holes, respectively [6,7]. It is worth noting that the minimum value for the conductivity of the fast-charging electrode is $5 \times 10^{-5} \text{ S cm}^{-1}$ that guarantees the battery to reach 60% state of charge (SOC) at 10 C [11]. Electrodes with excellent electrical conductivity facilitate electron transport during charging and discharging, which play important roles in improving the rate capability of the batteries. The research focus is mainly on the design of electrode materials (doping, coating and structural design, etc.) to improve the electron transfer of the electrodes [12].

Another limiting factor for fast charging is the charge transfer overpotential. If the overpotential exceeds a certain critical value, degradation processes may occur on the anode (Li inventory loss) and cathode side (gas evolution), resulting in reduced battery life. The voltage of the battery (V) satisfies $V = V_{\text{oc}} + \delta_{\text{qa}} + \delta_{\text{qc}}$, where V_{oc} is the open circuit voltage, and δ_{qa} and δ_{qc} represent the overpotentials on the anode side and the cathode side, respectively. During battery operation, Li^+ ions are transported back and forth, and δ_φ can be further considered as the sum of the overpotentials of driving solid-state diffusion, electrode interface charge transfer, and ion transport in electrolyte.

Usually, the ionic conductivity of the material is mostly significantly lower than electronic conductivity. Therefore, the overpotential is mainly caused by ion transport. The Li^+ ions transport follows the

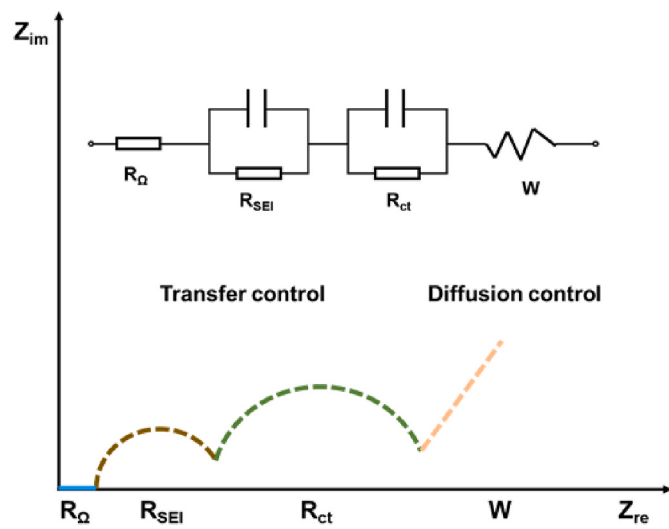


Fig. 1. Schematic diagram of AC impedance.

Arrhenius equation, namely $D_i = D_0 \exp(-\Delta G/(K_B T))$, where D_i represents Li⁺ ions coefficient, D_0 is the prefactor estimated empirically, ΔG is the energy potential difference, and K_B is the Boltzmann constant. Further, Li⁺ ions diffusion time (t) in the solid-state materials can be expressed as $t = x^2/(qD_i)$, where x represents the Li⁺ ions diffusion distance in materials, q is the dimensionality constant, which is 2, 4, and 6 for 1D, 2D, and 3D diffusion, respectively [13]. Under high current densities, Li⁺ ions will be deposited at the electrode interface if Li⁺ ions transport rate is lower than electron transfer rate, leading to the battery capacity loss and even to safety hazards. Generally, Li⁺ ions transport rate in material increases by increasing temperature (T), reducing the particle size (x) and adjusting the microstructure (q) to achieve fast Li⁺ ions diffusion [14,15].

3. Anode materials

An important limiting factor for fast-charging batteries is the inability of ions/electrons to transfer quickly into the anode material. According to the energy storage mechanism, anode materials can be divided into intercalation-type, conversion-type and alloy-type materials. In addition, some anode materials have more than one charge storage mechanism at the same time, such as porous carbon, transition metal dichalcogenides, and nanomaterials. In the process of Li storage, Li⁺ ions transfer and bulk phase diffusion in anode materials are mainly driven by local electric field and concentration gradient, respectively, which are the key factors determining the fast-charging capability. In the following sections, we mainly focus on carbon-based materials, lithium titanate and silicon-based materials as the most valuable and promising fast-charging anode materials.

3.1. Graphite anode

3.1.1. Graphite

Graphite is an ordered graphene layer stacked in ABABA with appropriate interlayer spacing (0.335 nm) capable of allowing reversible Li⁺ ions intercalation/deintercalation. Graphite was first used as an anode material for lithium batteries by Yazami group [16], and it was successfully used in commercial electrochemical devices in 1991. The intercalation process of Li⁺ ions can generally be described as $xLi^+ + xe^- + C \rightleftharpoons Li_xC$, showing a theoretical capacity of 372 mAh/g. Since then, graphite has been the best choice for commercial lithium-ion battery anode material due to its good reversibility, safety, and relatively low cost. However, graphite has slow Li⁺ ions intercalation kinetics and low lithiation voltage (~0.1 V vs Li⁺/Li), which seriously hinder its practical application. At high current densities, Li⁺ ions that are not inserted into the graphite layer will be deposited on the graphite surface due to the slow kinetics. Ho et al. [17] built a cell for conducting high-resolution *in situ* X-ray microtomography experiments to quantify three-dimensional lithiation inhomogeneity and lithium plating. Konz et al. [18] first observed the effects of energy density, charge rate, temperature and state of charge on lithium plating by using simple, accessible and high-throughput cycling techniques, refining a mature physics-based electrochemical model and providing an interpretable empirical equation to predict the plating onset state of charge. The deposited active Li metal undergoes side reactions, resulting in rapid capacity decay and serious safety issue. The thermal runaway characteristics of commercial batteries degraded by increasing charging current were analyzed by ARC and NMR tests [19]. Due to the reaction between the plated lithium and the electrolyte, a decrease in thermal runaway trigger temperature (T_2) to 103.9 °C was observed on cells charged at high rates, lower than the T_2 of 215.5 °C for cells charged at low rates, revealing the role of lithium plating in the triggering of thermal runaway. Considerable efforts have been done to rapidly intercalate Li⁺ ions into graphite to eliminate Li dendrite formation during fast charging [20–22]. For example, the overpotential of Li metal nucleation on lithiated Au is almost zero. Yan et al. [23] used a

functional separator of Au nanoparticle layer to adjust the lithium plating position during fast charging, ensuring high battery safety without affecting the energy density of lithium batteries.

Besides, researchers have developed several strategies to improve the electrochemical performance and rate capability of graphite electrodes, such as shortening the diffusion path, enlarging the graphite interlayer spacing, interfacial modification. Zhang's group [24] recorded the real behavior of nanoscale turbostratic carbon-coated graphite using a three-electrode system. The abundant active sites and the additional fast Li⁺ ions diffusion path located on the basal side of the graphite sheet can reduce the polarization in the charging process, which is beneficial to improve the rate capability of the graphite anode. Based on density functional theory (DFT) calculations, the energy barrier of Li⁺ ions through the C₆ ring (~10.2 eV) is much higher than that of through graphite interlayer spacing (~0.6 eV), so the intercalation of graphite occurs mainly through the edge plane rather than through the basal plane [25,26]. The Li⁺ ions must be embedded from the edge sites and gradually diffuse into the interior of the particles, resulting in a longer diffusion path, a lower Li⁺ ions diffusion rate and poor rate performance. Therefore, graphite with more edge sites and thus larger surface area has a trade-off between fast charging behavior and increased initial capacity loss.

By optimizing the morphology and structure of graphite, its fast-charging capability can be effectively improved. Creating pores in graphite is an effective method to shorten the Li⁺ ions diffusion path and improve the fast-charging performance. Cheng et al. [27] used strong alkali (KOH) to etch on the graphite surface to generate nanopores, so that Li⁺ ions could not only enter from the graphite edge plane, but also be embedded from the base plane, which shortened the migration path, exhibiting better rate performance than pristine graphite (Fig. 2a). However, mild conditions must be used, otherwise many pores will collapse and cannot be used as Li⁺ ions diffusion channels. Lim et al. [28] prepared porous graphite foams (GFms) using mesophase pitch, which increased the diffusion channels of lithium ions and achieved a capacity retention rate of 92% at 30 C versus 0.2 C (Fig. 2b). Billaud et al. [29] reported a superparamagnetic iron oxide particle-coated graphite to obtain an ordered structure perpendicular to the current collector by adjusting the magnetic field orientation, which could fully expose the active sites and shorten the Li⁺ ions diffusion path, exhibiting three times higher capacity than randomly oriented electrodes at 2 C rate.

Enlarging the graphite interlayer spacing is another effective way to increase the lithium diffusion rate. Guo et al. [30] used hydrogen peroxide to obtain micro-expanded layered spherical graphite. The interlayer spacing of micro-expanded layered graphite (0.336 nm) was slightly larger than that of spherical graphite (0.335 nm), which was beneficial to the diffusion of lithium ions, and showed excellent capacity retention (96.9%) at 2C rate than pristine graphite (94.5%). In addition, the functionalized graphite containing O, H, N and other elements on the surface can not only increase the interlayer spacing, but also form hydrogen bonds with solvent molecules and reduce the activation energy of Li intercalation [31]. With the synergistic effect of *d*-spacing and functional group enlargement, regraphitized natural graphite exhibits enhanced capacity, especially in high-rate applications [32]. Ou et al. [33] carefully designed graphite with active edges through a controlled solution treatment and sintering process. The active edges of the curved region coexisted with additional intercalation sites and expanded layers, which could effectively reduce the polarization during charging by improving the intercalation ability, thereby achieving a superior reversible capacity of 150.3 mAh/g at a high rate of 10 C (1C = 370 mAh/g).

In addition, the hidden value of developing spent graphite anodes in a sustainable approach was investigated to balance ore resource consumption and toxic/carbon emissions. The green Flash Joule heating (FJH) method developed by Dong et al. could provide a large current for defect repair and crystal structure reconstruction in graphite, making

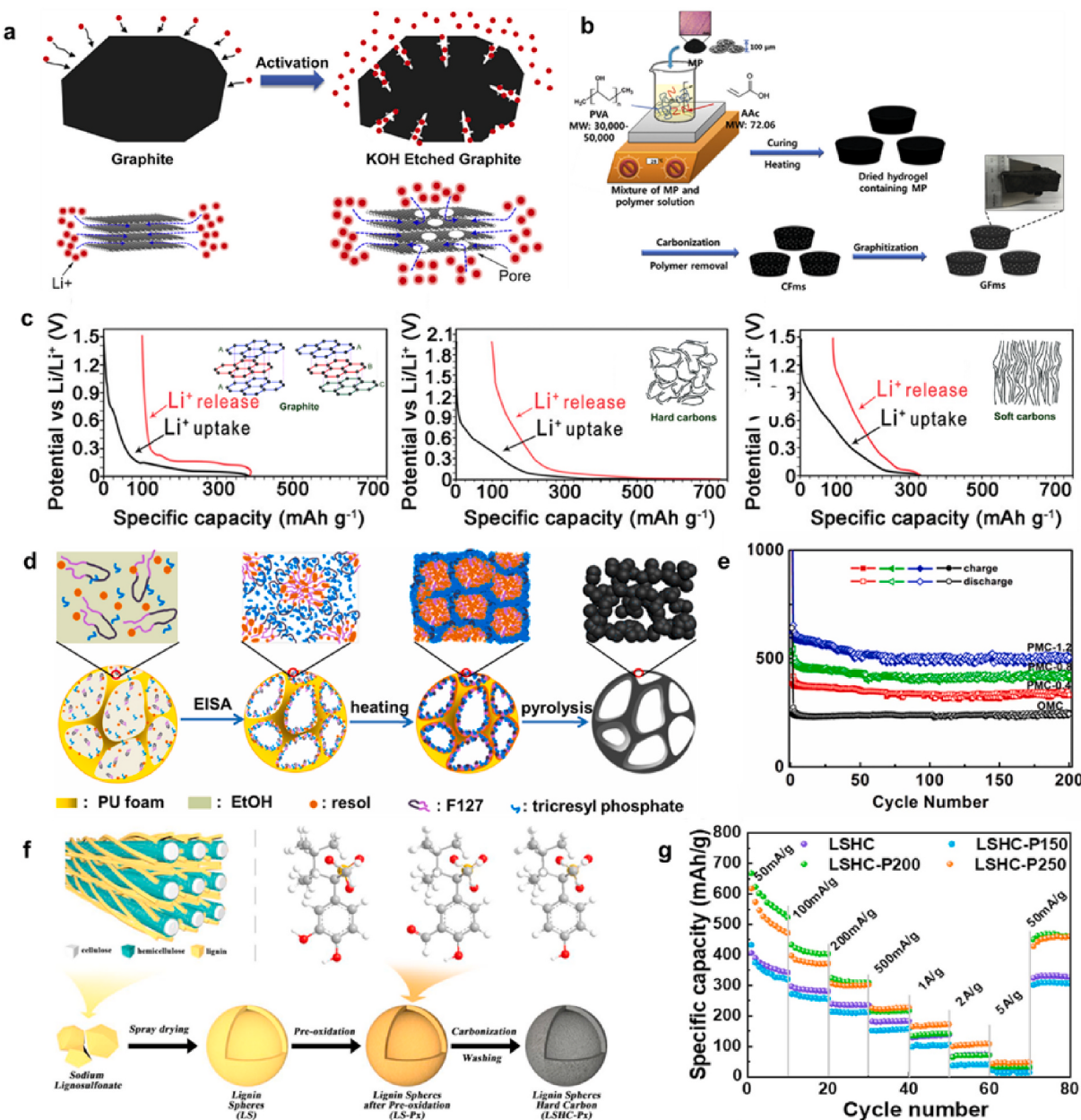


Fig. 2. (a) Schematic representation of pristine and KOH-etched graphite [27]. (b) Fabrication process of GFms [28]. (c) The discharge/charge curves of graphite, hard carbons and soft carbons [41,42]. (d–e) The formation process of large pore P-doped mesoporous carbons (d) and cycling performances at a current rate of 0.5 C of the pristine ordered mesoporous carbon (OMC) and the P-doped mesoporous carbon of PMC-0.4, PMC-0.8 and PMC-1.2 (e) [47]. (f–g) Schematic illustration of hard carbon preparation process (f) and the rate capacity of lignin-based hard carbons obtained at different pre-oxidation temperatures (g) [48].

recycled graphite even superior to new commercial graphite in terms of electrical conductivity [34]. Based on deep understanding and rational use of lithiation-induced structural evolution to aid regeneration, Yao et al. [35] developed a scaled-up delamination protocol to weaken van der Waals bonded graphite interlayers with the help of in situ generated H_2 bubbles and $\text{Na}_2\text{Ti}_3\text{O}_{13}$ (NTO) nanosheets for interfacial modification. Through electrostatic self-assembly of recycled few-layer graphene and electroactive NTO nanosheets, the constructed layer stacks exhibited impressive cycle durability even at 10 C (75% capacity retention after 2000 cycles).

3.1.2. Other carbon materials

In addition to graphite, carbonaceous anodes including hard and soft carbons have also been investigated as anodes for high-performance lithium batteries. The advantages of hard and soft carbon over

graphite as anode material lie in the expansion of interlayer spacing, rich edges, and abundant voids for Li-ion transfer and storage.

The generalized carbonization process can be divided into pyrolysis, carbonization and graphitization process. If the decomposition product is in a semi-fluid state, it is easily graphitized to form soft carbon, and its structure gradually evolves to a graphite structure at high temperatures up to 3000 °C. However, for carbon-based precursors with fully cross-linked nanostructures, graphitization is difficult even above 3000 °C, which is called hard carbon [36]. According to advanced characterization techniques, hard carbons with a “house of cards” structure have short-range graphitization regions with higher extended interlayer distances (>0.37 nm) than soft carbons (0.36–0.37 nm) and graphite (0.335 nm), which can improve the diffusion rate of Li^+ ions [36–38]. Besides, both hard and soft carbons are characterized by a large number of randomly distributed curved graphite sheets, inducing the formation

of nanovoids/pores, edges and defects, which can effectively shorten the Li^+ ions transport distance and provide abundant active sites and fast charge transfer reactions [39,40]. These properties not only improve the specific capacity but also help to realize fast charging for the batteries.

Furthermore, the Li^+ ions intercalation/deintercalation reaction mechanisms of carbon materials with different degrees of graphitization are different. More specifically, the charge-discharge curves are different, as shown in Fig. 2c [41,42]. Generally, the storage of lithium in carbon-based materials can be divided into the absorption of Li^+ ions at defect sites or nanovoids/pores, and the intercalation of Li ions into the graphite layer, where each stage corresponds to the different voltage region. Although a lot of research work has been done on the lithium storage mechanism in carbon-based anode materials, the intercalation-deintercalation mechanism is still controversial due to their complex microstructure, which mainly includes “adsorption-intercalation” mechanism and intercalation-adsorption” mechanism [43]. Compared with graphite, hard carbon does not show any distinct plateaus on the discharge/charge curves, and the electrochemical intercalation of Li^+ ions is around 0.8 V versus Li^+/Li ; while soft carbon has a higher onset voltage of 1.0 V and no apparent low voltage plateau compared to other carbon-based materials. Moreover, soft carbon presents a higher starting voltage of 1.0 V versus Li^+/Li than other carbon-based materials that have no obvious low voltage plateaus. The average voltage is closely related to battery energy density, and the low intercalation potential of the graphite material helps the battery to obtain a high energy density. Although soft carbon shows higher electronic conductivity, it appears to be less attractive in commercial electrochemical devices than hard carbon because of its high operating voltage and less competitive interlayer spacing.

The unique structure of hard carbon allows more Li^+ ions to be stored, thus showing a higher specific capacity than graphite (400–1000 mAh/g vs. 372 mAh/g). However, a large number of edge sites affect solid state interface (SEI) film formation and the Li ions trapped in nanovoids reduce the amount of reversible Li, which lead to massive irreversible capacity loss. The microstructure and electrochemical properties of hard carbon are closely related to the precursor used and synthesis conditions. Therefore, it is necessary to select suitable raw materials and optimize the preparation process to attain hard carbon materials with high comprehensive performance [44]. Hard carbons used as anodes for LIBs are mainly derived from resin-based, pitch-based, and biomass-based precursors. Ni et al. [45] reported a hard carbon anode prepared from phenolic resin and obtained a specific capacity as high as 526 mAh/g (about 40% higher than graphite) with an initial coulombic efficiency of 80%, and the constructed $\text{Li}(\text{Ni}_{1/3}\text{C}_{0.1/3}\text{Mn}_{1/3})\text{O}_2/\text{hard carbon}$ full cell showed superior capacity retention (90%) at a discharge rate as high as 30 C.

Heteroatom doping in hard carbon can tune the structure and surface chemistry of anode materials. Qie et al. [46] fabricated nitrogen-doped hard carbon as anode for LIBs, and obtained superhigh capacity and rate capability. The specific capacity was as high as 943 mAh/g even at high current density of 2 A/g after 600 cycles. The superhigh capacity could be ascribed to the large number of N-doping derived active sites for Li storage like “lithium-ion reservoir”, while the excellent rate capability was caused by the enhanced electronic/ion conductivity. Wang et al. [47] reported a facial method for large-scale production of P-doped mesoporous carbons, which exhibited a high reversible capacity of ~500 mAh/g after 200 cycles at 0.5C rate. Due to the hydrophobic character of tricresyl phosphate, it induced a change in the micellar structure during the self-assembly process, which enlarged the pore size of the material from 3.6 to 14.2 nm, and the interlayer spacing from 0.368 to 0.379 nm, while increased the degree of graphitization of the carbon framework (Fig. 2d and e). However, the composition of the pitch precursor is complex and the mechanism of cross-linking and oxidation is unclear, making it difficult to become a candidate for hard carbon materials.

Compared with other carbon-based materials, biomass-based hard

carbons using biomaterials as raw materials can reduce the preparation cost, thereby bringing huge economic benefits. Biomass-based hard carbon has a unique structure in terms of composition, morphology and nanostructure due to the different types of precursors and preparation processes. Du et al. [48] employed a facile low-temperature pre-oxidation combined with post-carbonization strategy to prepare hard carbons with lignin as precursor. They demonstrated that carbonaceous intermediates with different configurations could be obtained by adjusting reaction temperature under air atmosphere, and obtained the highest carbonyl content at 200 °C, which corresponding product LSHC-P200 showed the best electrochemical performance with a reversible capacity increased from 347 to 584 mAh/g at 50 mA/g compared to directly carbonized samples (Fig. 2f and g). Notably, the native morphology of biomass-derived carbon materials could be well maintained after carbonization using cross-linking agents. It was reported that the introduction of $(\text{NH}_4)_2\text{HPO}_4$ promoted the dehydrogenation reaction of starch, and the further formation of $\text{C}-\text{O}-\text{PO}_3$, $\text{C}-\text{P}-\text{O}_3$ and $\text{C}_2-\text{P}-\text{O}_2$ played a key role in the cross-linking of polycyclic aromatic hydrocarbon unit fragments into graphite crystals, which facilitated the preservation of carbon materials with desired structure and properties [49]. Li et al. [50] prepared spherical hard carbon by one-step programmed heating of potato starch under inert atmosphere, which showed stable cycling performances and good rate capability as anode materials for LIBs. Du et al. [51] fabricated lithiophilic hard carbon-riveted graphite (HCRG) anode to meet the requirement of fast charging. Lithophobic to lithiophilic transition can attract more Li^+ ions and facilitate the reintercalation of Li^+ ions into the graphite block during the relaxation time at low potentials instead of plating on the surface, exhibiting excellent rate performance with 98.2% capacity retention when the rate increased from 1 C to 15 C and fast-charging performance with 90.1% energy retention after 4000 cycles at an ultrahigh rate of 10 C in $\text{LiFePO}_4/\text{HCRG}$ full cell.

Carbon-based materials have been widely studied as anode materials for fast-charging lithium batteries due to their simple preparation method, large specific surface area, easily tunable structure, and high electron transport ability. As a promising conductive substrate, carbon-based materials are structurally classified from one-dimensional (1D), two-dimensional (2D) to three-dimensional (3D) [52]. Different dimensions of materials with unique physical/chemical properties also have different advantages for fast-charging LIBs. Generally, 1D carbon structures such as nanorods, nanoneedles and nanowires can reduce the strain during volume expansion and contraction [53], 2D carbon with sheet, microtubule, and thin film morphologies have large specific surface areas to establish stable SEI and to promote uniform Li deposition to avoid dendrite [54], and 3D carbon materials with porous carbon channels can facilitate the transport rates of ions and electrons [55]. Chemical vapor deposition (CVD), direct top-down approaches, and hydrothermal reactions are commonly employed to construct fast-charging carbon anode materials with different dimensions. Holtsteige et al. [56] successfully prepared carbon nanospheres (CS) particles with different particle sizes by hydrothermal synthesis using glucose as precursor, and studied in detail their fast-charging capability as anode materials for LIBs. The results show that CS particles have very good long-term cycle stability, and the capacity retention can reach 89% after 8000 cycles at 10 C rate. However, carbon-based materials in batteries usually suffer from large initial capacity loss due to undesired side reaction caused by their defective structures. Therefore, most of them are often used as conductive additives to improve electron transfer in electrodes due to their excellent electrical conductivity.

3.2. Lithium titanate anode

$\text{Li}_4\text{Ti}_5\text{O}_{12}$ (LTO) is another anode material, which shows good cycling stability, high rate capability and safety, and low-temperature performance [57]. The LTO with cubic space group Fd-3m can be represented as $[\text{Li}_3]^{8a}[\text{Li}_1\text{Ti}_5]^{16d}[\text{O}_{12}]^{32e}$, where Li ions occupy the

tetrahedral 8a site and one sixth of the octahedral 16d site, and the remaining 16d sites are occupied by Ti [58]. After lithiation, three Ti^{4+} are reduced to Ti^{3+} , and Li^+ ions occupy 16c site and push the original Li^+ at 8a site to move to 16c site, forming the rock salt structure of $\text{Li}_7\text{Ti}_5\text{O}_{12}$ ($\text{Li}_3^{16c}[\text{Li}_1\text{Ti}_5]^{16d}[\text{O}_{12}]^{32e^-}$) [59]. Thus, the insertion process can generally be expressed as $\text{Li}_4\text{Ti}_5\text{O}_{12} + 3\text{e}^- + 3\text{Li}^+ = \text{Li}_7\text{Ti}_5\text{O}_{12}$, giving a theoretical capacity of 175 mAh g^{-1} . From the perspective of LTO structure, although its 8a site is not as energetic as the 16c site, it can also accommodate Li^+ ions. An et al. [60] extended the LTO discharge cut-off potential to near 0 V, and the reversible capacity approached 250 mA h g^{-1} , exceeding the generally accepted theoretical capacity of 175 mA h g^{-1} . Because low discharge voltage may lead to structural instability and SEI formation, and Li intercalation occurs at a voltage of about 1.55 V, which limits its application at high cut-off voltages above 1 V, and hence avoids electrolyte consumption and reduces interfacial charge transfer resistance. Furthermore, the strong Ti-O bond stabilizes its structure with a lattice shrinkage of only 0.77% during the two-phase transition, also known as a “zero-strain” material. The LTO anode can overcome the shortcomings of graphitic anodes such as the formation of dendritic lithium and unstable solid-electrolyte interface during charging, which is crucial for improving the cycling stability and operational safety of LIBs. Electrochemical and safety properties of LTO and graphite anodes paired with LiMn_2O_4 cathodes in pouch cells demonstrated that LTO anode outperformed graphite in capacity retention, pulse resistance, and calendar life over extended cycles [61]. As a promising anode for Li-ion battery, the LTO has been used successfully in EVs and energy storage markets [62].

Although LTO is very promising as an anode material for LIBs, the low intrinsic conductivity ($\sim 10^{-13} \text{ S/cm}$) and slow Li^+ diffusion kinetic ($10^{-13}\text{-}10^{-8} \text{ cm}^2 \text{ s}^{-1}$) limit further improvement in fast charging performance [63–65]. Additionally, the outgassing issues remain challenges for large-scale commercial applications. Although the cause of gas evolution (e.g., CO_2 , H_2 , CO) in LTO is still debated, many researchers have proposed that gas evolution is mostly caused by reactions

at the interface between LTO electrodes during initial cycling. In addition to the trace water that promotes the decomposition of the electrolyte to produce gas, the mechanism of gas generation may also be that the surface of LTO may promote the decomposition of the electrolyte, including the dehydrogenation and decarboxylation of alkoxy groups in the electrolyte [66]. The rate performance and gassing problems of LTO have been improved by various methods, mainly including surface modification, doping and morphology control at the electrode material level [67].

Generally, surface modification on LTO is a widely accepted method to increase rate capacity due to easy preparation and wide availability. Among several suitable candidates, carbon has attracted great interest because various carbon sources can be directly mixed with LTO or its precursor materials followed by high temperature heat treatment. Graphene-based materials have high electrical conductivity, thermal conductivity, and mechanical strength, and the 3D framework can facilitate ion and mass transport, so it shows great potential for application [68,69]. Chen et al. [70] prepared $\text{Li}_4\text{Ti}_5\text{O}_{12}$ with a conductive network structure by using graphene. The graphene not only acts as a conductor component to bridge the conduction between LTO and current collector (1.0 S/cm), but also improves ion diffusion kinetics due to 3D channels ($\sim 3.6 \times 10^{-12} \text{ cm}^2/\text{s}$) (Fig. 3a). Similarly, carbon nanotubes (CNTs) can also help improve the electronic conductivity of LTO [71, 72]. Li et al. [73] synthesized mesoporous LTO nanoclusters in CNT network frameworks by a solution-based approach, in which CNT served as frameworks to support binder-free electrodes, and made the composites highly conductive and flexible. Such free-standing LTO@CNT electrode enabled the composite anode with an ultra-high capacity of 173.9 mAh/g at 0.5 C, a high rate capability of 164.3 mAh/g even at 20 C, and impressive cycling stability of 89% after 1200 cycles at 1 C [73]. In addition, various organic carbon precursors can be used to prepare high-rate $\text{Li}_4\text{Ti}_5\text{O}_{12}$ anode materials because organic carbon precursors are easy to form a uniform and thickness-controllable carbon film on the surface of $\text{Li}_4\text{Ti}_5\text{O}_{12}$ particles during the pyrolysis process [74,75]. Wang

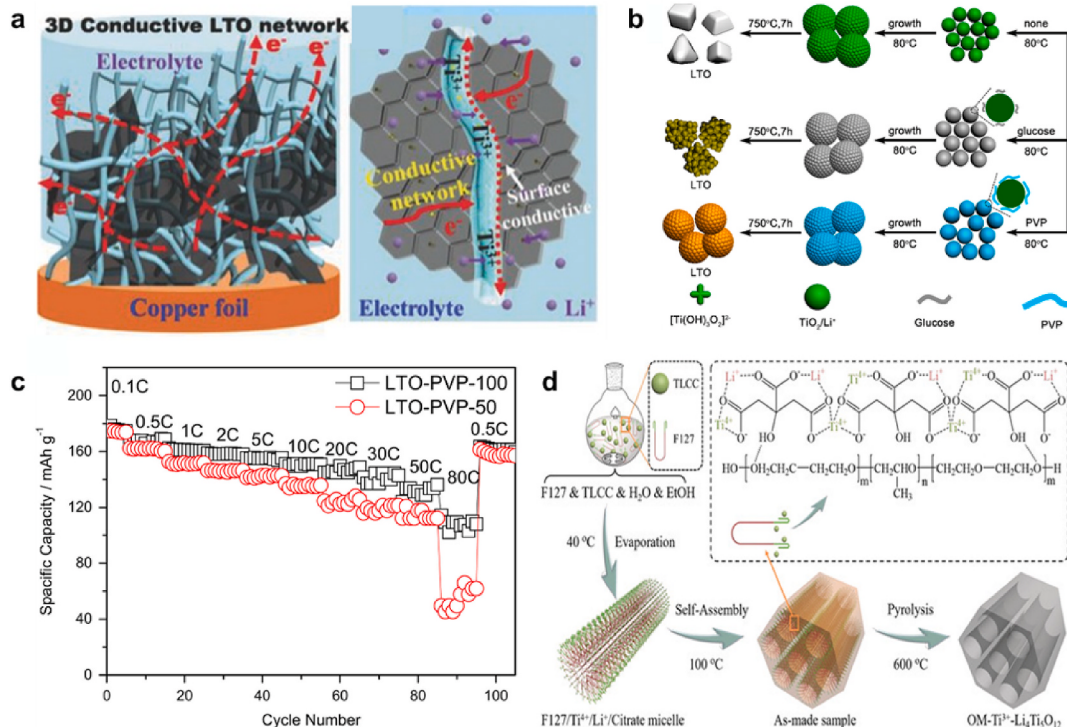


Fig. 3. (a) Schematic illustration of a 3D conductive LTO network electrode and its electron and Li^+ transport paths for ultrafast charge-discharge [70]. (b–c) Schematic illustration of in-situ synthesis of $\text{Li}_4\text{Ti}_5\text{O}_{12}/\text{C}$ using different carbon sources [76]. (d) Illustration of the construction of the OM- Ti^{3+} - $\text{Li}_4\text{Ti}_5\text{O}_{12}$ through the stoichiometric cationic coordination assembly process. TLCC is the synthesized $\text{Ti}^{4+}/\text{Li}^+$ -citrate chelate [78].

et al. [76] developed a robust strategy for the synthesis of monodisperse LTO nanospheres with an average diameter of 120 nm by using titanium nitride (TiN) as the titanium source and polyvinylpyrrolidone (PVP) as the carbon source. The in situ formed PVP layer kept the LTO monodisperse with spherical morphology after annealing (Fig. 3b and c). The as-prepared monodisperse LTO nanospheres with an average size of 15 nm uniformly coated by a carbon layer exhibited a high tap density (1.1 g/cm³) and an outstanding rate-cycling capability (108.9 mAh/g at 80 C). In addition, other coatings, such as metals, oxides, and fast ionic conductors, and heterogeneous (special impurity phases) have also been applied to improve the rate capability of LTO [59]. Rutile/anatase TiO₂ as a precursor for LTO synthesis showed a higher theoretical capacity of 336 mAh/g and a faster Li⁺ intercalation/deintercalation rate than LTO [77]. Wang et al. [78] synthesized a mesoporous spherical Li₄Ti₅O₁₂/TiO₂ composite and obtained a high rate capability with a capacity of 111 mAh/g at 20 C and a stable cyclability with 93.04% capacity retention with 145 mAh/g after 120 cycles at 2 C (Fig. 3d). Since the gas is generated by the interfacial reaction of LTO, the key point for solving the outgassing problem should be to avoid direct contact between LTO and the electrolyte.

Elemental doping is another important method to improve the intrinsic electronic/ionic conductivity of Li₄Ti₅O₁₂ by introducing defects or vacancies [79]. Many anions and cations can be doped into the crystal structure of Li₄Ti₅O₁₂ by substituting 8a tetrahedral Li sites, octahedral 16d Ti sites or oxyanion sites to form various phase structures and improve the original properties. In addition, different dopants prefer different doping sites and have different effects on phase structure. In general, partial substitution of Li by +1 valent dopant ions with large ionic radius such as Na⁺ and K⁺ in the tetrahedral 8a sites can increase the capacity by expanding the lattice of LTO to accommodate more Li⁺ ions in the enlarged lattices [80]. Increasing the lattice parameters without compromising the lattice stability is beneficial to reduce charge transfer resistance (229.7 Ω) and improve Li⁺ ions diffusivity (2.39×10^{-16} cm²/s). Yi et al. [81] synthesized single-phase Li_{4-x}Na_xTi₅O₁₂ ($x \leq 0, 0.05, 0.1, 0.15, 0.2$) spinel by a simple solid-state method, and the discharge capacity of Li_{3.85}Na_{0.15}Ti₅O₁₂/Li cell was 135 mAh/g after 200 cycles at a high charge-discharge rate of 5 C. And some dopant ions with larger atomic radius or higher valence (such as Cr³⁺, Gd³⁺, Mn⁴⁺, Mo⁴⁺, Ta⁵⁺, etc.) can also improve the discharge capacity of modified LTO materials by substituting part of Ti⁴⁺ at the octahedral 16d site [82–85]. Doping transition metal ions can create oxygen vacancies that greatly increase ionic conductivity by narrowing the band gap between the occupied O-2p state and the vacant Ti-3d state in LTO [86–88]. Xu et al. [89] synthesized gadolinium doped and carbon-coated ultrathin LTO nanosheets (denoted as LTO-Gd-C) for enhanced lithium storage. Owing to the synergistic effect of Gd doping and carbon coating, the Li⁺ ion diffusion coefficient of LTO-Gd-C is 6.03×10^{-11} cm²/s, which is much higher than that of the undoped LTO electrode of 4.60×10^{-12} cm²/s, showing an excellent rate performance of 171 mAh/g at a high rate of 10 C. Furthermore, replacing the oxygen 32e sites with electron-donating anions such as F⁻ or Br⁻ in LTO induces the formation of charge-compensating Ti³⁺ in addition to enhancing the electronic conductivity [90,91]. Through theoretical calculations, the researchers predict that Br⁻ can significantly reduce the size of the band gap, thereby facilitating electron transport in the LTO lattice. Besides, the electronic conductivity of LTO can also be enhanced by exploiting the synergistic effect of co-doping of high-valent transition metal and halide ions. Ji et al. [92] showed that the improved electrochemical performance of LTO can be attributed to proper co-doping with La³⁺ and F⁻, which can increase the mixing amount of Ti³⁺/Ti⁴⁺ as charge compensation, thereby reducing charge transfer resistance and improving electronic conductivity and Li⁺ ion diffusivity. Furthermore, the synergistic effect of further cationic doping or carbon coating endows the composite with an efficient Li⁺ diffusion channel and electronic conduction network, resulting in remarkable rate capability [93–95].

Alternatively, other approaches, such as preparing nano-sized LTO, incorporating pore structures, or controlling morphology have been employed to improve the rate performance. Various nanoscale morphologies of LTO, such as nanotubes [96], nanowires [97], and nanosheets [98], showed excellent rate performance when used as anode materials. The nanoscale morphologies of LTO can reduce the diffusion distance of Li⁺ ions and electrons within the bulk of the electrode material. In addition, the nanostructure increases the surface area, which is available for interfacial charge transfer [99]. A novel oxygen-deficient TiO₂/Li₄Ti₅O₁₂ biphasic heterostructure nanosheet was successfully synthesized and used as an anode material for LIBs, exhibiting extraordinary rate capability with a capacity of 174 mAh/g at 200 C and excellent long-term cycling stability with only a 6% decrease in capacity after 6000 cycles [100]. However, nanoscale materials have some practical limitations due to their low tap density. In addition, some novel 3D structures, such as hierarchical pores, hierarchical spheres, and mesoporous structure, have received special attention because they not only can increase the tap tensile of the materials but also minimize the length of diffusion paths and thus positively affect the rate performance and energy density of LTO batteries [78,101,102]. For example, Tang et al. [103] introduced a facile method to synthesize LTO microbars with micropores created by ammonium bicarbonate as a template. The as-prepared LTO microbars exhibited a very low specific surface area (6.11 m²/g), high ionic conductivity (5.53×10^{-12} cm²/s), large tap density (1.20 g/cm³), exceptionally stable long-term cycling performance (94.0% after 500 cycles at 10 C), and excellent rate capability (129.3 mAh/g at 30 C). Wang et al. [104] reported nanosheet-assembled LTO hierarchical microspheres with controlled features at the nano- and micro-scale, which enabled dense particle packing (1.32 g/cm³), easy Li⁺ ions diffusion (1.89×10^{-11} cm²/s) and high structural robustness, and offered extremely high rate capability (155 mAh/g at 50 C) and excellent cycling stability (99.5% capacity retention after 2000 cycles at 50 C and 95.4% capacity retention after 3000 cycles at 30 C). Therefore, controlling the synthesis conditions and tuning the morphology are crucial to improve the tap density and rate capability of LTO, which is very important for its practical application. Additionally, due to its high cost, LTO may be more suitable for practical application in some special areas.

3.3. Silicon anode

Silicon has been intensively studied as a potential next-generation anode material for LIBs due to its abundant resource, high specific capacity (4200 mAh/g), and relatively low discharge potential plateau (0.4 V vs Li⁺/Li) [105–107]. With the industrialization of Si-based anode materials, the market demand gradually increases [108]. During the lithiation process, Li⁺ ions intercalate into Si particles and form a series of Si-Li phases (LiSi, Li₁₂Si₇, Li₁₃Si₄ and Li₂₂Si₅), which eventually lead to the incorporation of 4.4 Li⁺ ions into per Si atom but a volume expansion of approximately 420% [109]. The huge volume change creates a large internal stress, which eventually leads to the fracture and pulverization of Si particles. This is the big challenge to the design and manufacture of Si anode based LIBs. In addition, the low intrinsic conductivity of silicon (1.56×10^{-3} S/cm) also limits the improvement of its rate capability [110,111]. Modification of Si-based materials, including particle size reduction, design of new microstructure, and surface coating, has shown efficient in improving the performance of Si electrodes [112].

Reducing Si particle size can not only effectively alleviate the volume expansion during lithiation, but also shorten the Li⁺ ion diffusion path, thereby improving its rate capability. Si materials with different sizes and morphologies mainly include 0D materials (such as hollow Si spheres and porous Si particles), 1D materials (Si nanowires, Si nanofibers, Si nanotubes, etc.), 2D thin film Si and 3D Si microstructures [113]. Although Si is designed with particles below a certain size to better accommodate volume change due to the large tolerance of tensile

stress, some special attention has been paid to recent efforts to micron-scaled Si, which may have greater commercial benefits. 3D Si structures are of great interest because they can not only retain the advantages of nano-Si, but also eliminate its associated disadvantages, such as low tap/pressing density, and low Coulombic efficiency. Wang

et al. [114] reported a binder-free electrode that interconnected carbon-sheathed porous silicon nanowires into a coral-like network and exhibited high specific capacities (1200 mAh/g) over 500 cycles at an ultra-high charge rate of 7 C (Fig. 4a). The enhanced electrochemical performance could be attributed to the combination of interconnected

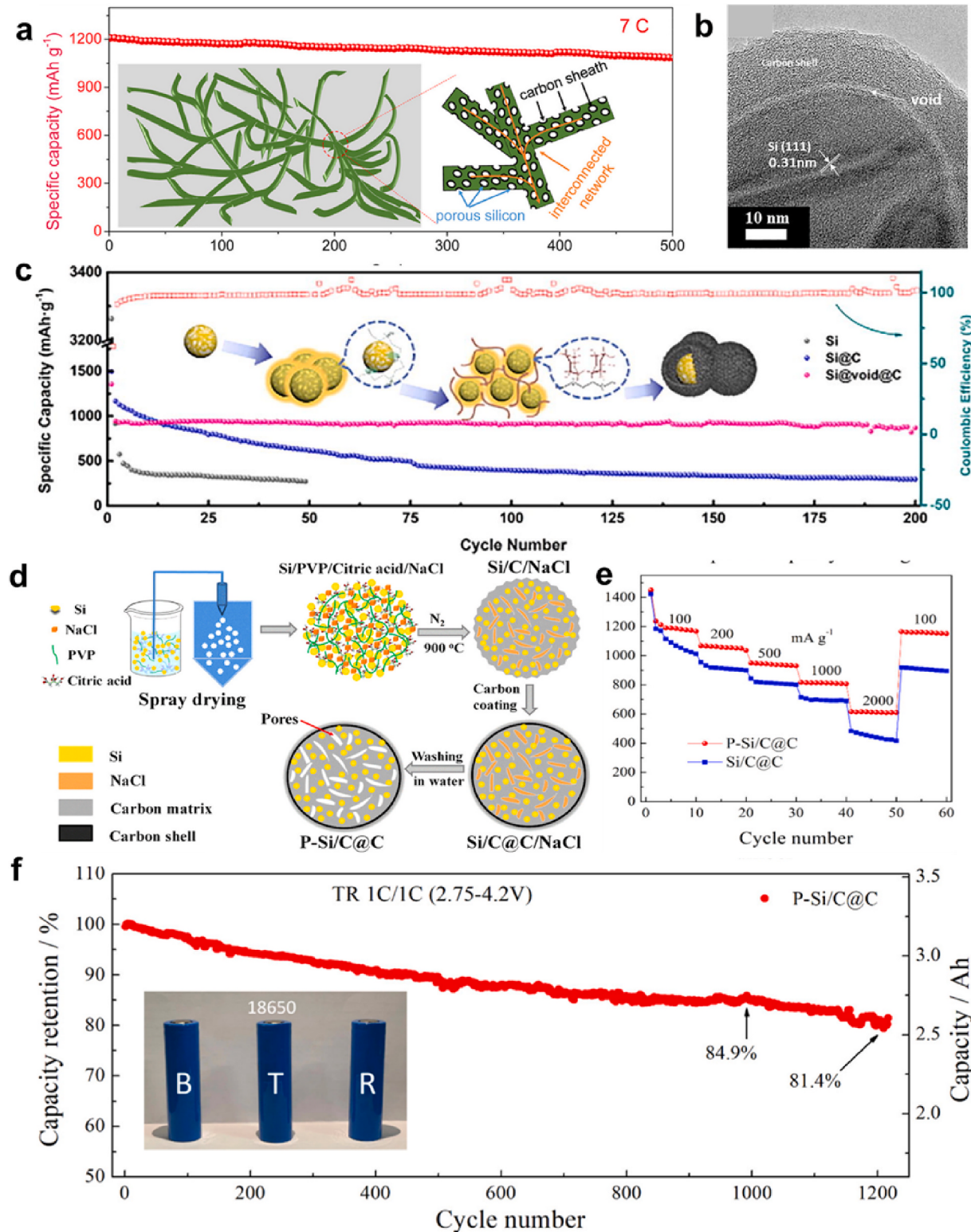


Fig. 4. (a) Schematic diagram of Si@C and cycle performance at 7C [114]. (b–c) TEM images of Si@void@C composites (b), and schematic illustration of fabrication route of Si@void@C composites and the cycling performance at the current density of 0.2 A/g (c) [118]. (d–f) Schematic illustration of the preparation process of P-Si/C@C microspheres (d), rate performance of P-Si/C@C and Si/C@C (e), and cycling performance of P-Si/C@C//NCA cylindrical cell (f) [120].

structure and improved electrical conductivity, which not only alleviates the volume change but also facilitates the reaction kinetics of the Si anode.

Surface coating is an alternative approach to improve the electrochemical performance of Si anodes. The core-shell Si@Li₄Ti₅O₁₂ nanocomposite prepared by Liu et al. took advantage of nanoscale Si particles and pure Li₄Ti₅O₁₂ (LTO) coating, and showed high initial discharge/charge specific capacities up to 1756/1383 mAh/g at 500 mA/g, high rate capability with 620 mAh/g at 4000 mA/g, excellent cycle stability (883 mAh/g after 150 cycles) and low volume expansion (only 3.3% after 150 cycles) [115]. Carbon-based materials have long been regarded as ideal coating agents for Si-based anodes, and the Si/C composites retain both the advantages of carbon and high capacity of Si. Ke et al. [116] developed scalable silicon nanolayers embedded in graphite/carbon hybrids (SGC) hybrids, in which silicon nanolayers were embedded in graphite/carbon and silicon nanolayers were uniformly grown on the surface and internal pores of graphite by a CVD process. The architecture achieved the compatibility of silicon with natural graphite, and solved the problem of severe side reactions caused by structural failure. The Coulombic efficiency was 92% at the first cycle and rapidly increased to 99.5% after only 6 cycles with a capacity retention of 96% after 100 cycles. In general, carbon-based matrix supports usually serve to provide a conductive network for Si active materials, and to accommodate the mechanical stress of Si during Li intercalation/deintercalation. In addition to improving the Si anodes through simple mixing of carbon precursors or adding carbon by pyrolysis, an improved synthetic route was also used to design special morphologies of silicon/carbon composites to address the stress caused by Si expansion/contraction [117]. Sun et al. [118] proposed a sacrificial templating strategy to synthesize yolk-shell Si@void@C composites by using polyethyleneimine to form void spaces during carbonation without acid or alkali etching (Fig. 4b and c). This unique structure can provide satisfactory voids for silicon expansion and more active sites for Li⁺ ions storage, delivering a capacity of 854.1 mAh/g after 200 cycles at a current density of 0.2 A/g capacity, and 510 mAh/g after 100 cycles at 1 A/g.

Currently, the market products are mainly concentrated to the Si-based anode materials with specific capacity of around 450 mAh/g. The anode manufacturers are eagerly developing various commercialized silicon-based anode materials, and continue to reduce production cost and promote the growth of the Si-based anode market [119]. Tesla's use of Si/C anode materials in Model 3 has driven the rapid expansion of the Si-based anode market. At present, there are two commercial technical routes for Si-based materials: Si/C composite material and SiO_x anode material. Some enterprises have reported that the capacity of the latest generation of Si/C anode material can reach 1500 mAh/g, and SiO_x is more than 1600 mAh/g. Because commercial pack batteries and square aluminum-shell batteries are still very sensitive to swelling, high-capacity Si/C materials may be mainly used in cylindrical batteries in the future. Zhang's group reported a large-scale synthesis of micro/nanostructured porous Si/C microspheres composed of Si nanoparticles tightly immobilized on a micron-scale cross-linked C matrix in cooperation with BTR enterprise (Fig. 4d-f) [120]. By virtue of structural advantages, the prepared Si/C anode exhibited a high initial Coulombic efficiency of 89.8%, a large reversible capacity of 1269.6 mAh/g at 100 mA/g, and excellent cycling performance (87.1% capacity retention after 820 cycles at 1000 mA/g). Furthermore, the material showed low swelling (18.1%) at a high areal capacity of 3.8 mAh cm⁻², and achieved 81.4% capacity retention even after 1200 cycles at 1 C when assembled into a 3.2 Ah cylindrical battery. Although the rate capability has few directly emphasized for the Si-based anode materials, it is generally acceptable from the numerous reports.

4. Cathode materials

From the perspective of the cathode electrodes, at high currents, an

inner particles stress due to the diffusion of Li⁺ ions are amplified generally, which will increase the heterogeneity and generate more stress throughout the battery operation, leading to the destruction of the material structure and the deterioration of the capacity. To improve the fast-charging performance of cathode materials, current strategies usually focus on building highly conductive pathways and constructing short Li⁺ ion diffusion paths. At present, the cathode materials such as LiMO₂, xLi₂MnO₃·(1-x)LiMO₂, Li₃V₂(PO₄)₃, LiMn₂O₄, LiFePO₄ etc. have been widely investigated [121,122]. Among them, LiFePO₄, LiCoO₂ and LiNi_xMn_yCo_zO₂ cathodes are main commercial cathode materials, so we will discuss their fast-charging design strategies.

4.1. LiFePO₄ cathodes

Due to its inherent advantages such as low cost, suitable voltage platform, and high safety, olivine LiFePO₄ has been considered as the most promising cathode material for LIBs used in EVs since it was discovered by Goodenough's group in 1997 [123–125]. The olivine-structured LiFePO₄ material belongs to the orthorhombic family, and its unit cell parameters are $a = 1.0334$ nm, $b = 0.6008$ nm, $c = 0.4694$ nm, in which the P atoms are located at the tetrahedral sites, and the Li and Fe atoms are located at the octahedral 4a and 4c sites, respectively [126]. It is worth noting that the delithiation phase FePO₄ has a similar structure to LiFePO₄, but its unit cell parameters are $a = 0.9821$ nm, $b = 0.5792$ nm, $c = 0.4788$ nm, and the unit cell volume is reduced by 6.8%. The small negative expansion of FePO₄ not only avoids the capacity drop caused by the drastic volume change during cycling, but also effectively compensates for the anode volume change during lithiation process. However, despite the commercial success of LiFePO₄ batteries in EVs, they are still hampered by material property limitations [127,128]. Because of the steric hindrance of PO₄³⁻ tetrahedra, LiFePO₄ can only provide a one-dimensional b-axis diffusion channel for Li⁺ ions, resulting in poor ionic conductivity (10^{-13} – 10^{-16} cm²/s) [129]. Besides, the low intrinsic electronic conductivity (10^{-9} – 10^{-10} S/cm) of LiFePO₄ is also the main disadvantage that limits its electrochemical performance and commercial application. Both are important parameters for fast charging. Thus, various methods have been proposed to overcome LiFePO₄ shortcomings to improve the performance.

Coating modification on LiFePO₄ particles is one of the most important and well-known strategies to improve its electrochemical performances such as capacity, cycle life and rate capability [130,131]. Among them, carbon coating on LiFePO₄ is a widely accepted method to improve the electronic conductivity. Meanwhile, carbon coating can not only reduce the particle size and particle aggregation of LiFePO₄, but also provide a reducing atmosphere to prevent Fe³⁺ from being oxidized to Fe³⁺ during the synthesis process [132–134]. In general, the traditional synthetic route involves mixing LiFePO₄ with various carbon precursors, which is facile and suitable for large-scale industrial production, but the carbon distribution in the LiFePO₄/C product is not so uniform [135]. And controlling the thickness of carbon is another key issue, since a thin and non-uniform coating cannot generate efficient electronic conductivity. If the carbon coating that is too thick, it will hinder the diffusion of Li⁺ ions and reduce the volumetric energy density of the LiFePO₄ batteries. So, the carbon coating thickness should be well balanced especially for fast charging. For example, Shi et al. [136] reported a thin and uniform porous carbon layer on LiFePO₄ (LiFePO₄/C) using polymer polyacrylonitrile block polymethyl methacrylate copolymer (PAN-*b*-PMMA) as carbon source (Fig. 5a). The obtained LiFePO₄/C composite maintains 78.9 mAh/g after 500 cycles at a very high current density of 30 C, which is mainly attributed to the multi-path transfer of Li⁺ ions and electrons provided by the porous carbon layer (Fig. 5b). In addition to the use of polymer precursors, various biomass-derived materials are employed as carbon precursors. Kim et al. [137] synthesized carbon-coated LiFePO₄ (C-LFP) with particles smaller than pure LFP (140 nm) and uniform particle size distribution (90 nm) by adding orange peel during the synthesis, and the

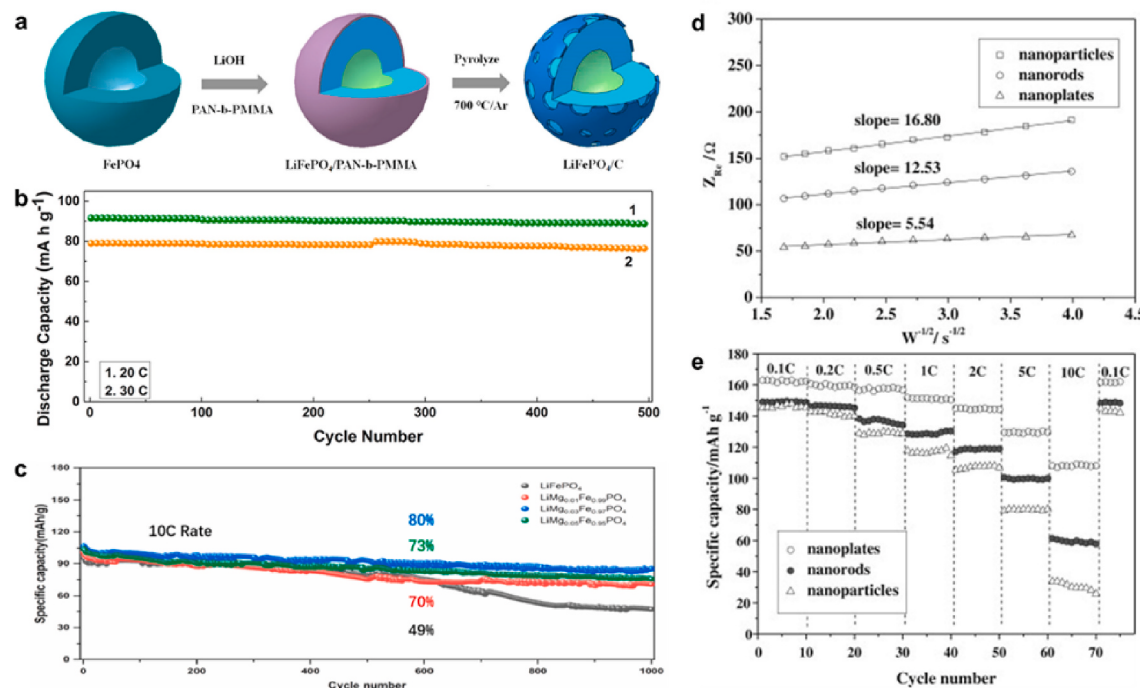


Fig. 5. (a–b) A scheme of the formation process of LiFePO₄/C (a) and its cyclic stability at different rates (b) [136]. (c) Cycling performance of LiFePO₄/C with different Mg doping amounts at 10 C [150]. (d–e) The relationship between Z_{RE} and $\omega^{-1/2}$ at low frequency (d) and the rate performances of LiFePO₄/C nanoparticles, nanorods and nanoplates (e) [158].

obtained C-LFP exhibited a high discharge capacity of 147.3 mAh/g at 0.5 C rate and 139.8 mAh/g at 1 C rate.

Doping is another important method to improve the intrinsic electronic/ionic conductivity of LiFePO₄ [138–140]. Replacing a small amount of Li⁺, Fe²⁺ or O₂[−] with heterogeneous ions is expected to enhance the capacity, cycle life and rate capability of LiFePO₄ batteries to some extent. Li-site doping has attracted great research interest since Chung et al. first reported that Li-site doping could enhance the electronic conductivity of LiFePO₄ [141]. However, doping may decrease the rate capability of LiFePO₄ if wrong dopant element is used. Wagemaker et al. [142] investigated the effect of aliovalent cation doping of LiFePO₄ with Zr, Nb and Cr elements on Li⁺ ion diffusion by using neutron and X-ray diffraction, and found that the dopants located in the internal Li⁺ ion channels would impede Li⁺ ion diffusion and hence reduce the rate capability. The controversial mechanism and effect of Li-site doping on electronic conductivity requires further investigation. Numerous works have focused on improving electrochemical performance of LiFePO₄ by heterovalent doping (e.g. Mo⁶⁺, Nb⁵⁺, and V⁵⁺) and divalent cations (e.g. Co²⁺, Ni²⁺, and Mg²⁺) replacing at Fe²⁺ sites [138,143–147]. Doping is usually accompanied by the generation of vacancies, defects and charge carriers, which are beneficial to improve the conductivity of materials [148]. Li et al. [149] reported a low-cost route to scale up the production of fast-charging LiFePO₄ materials by doping Zr⁴⁺ in Li-excess LiFePO₄, which facilitated electron transport by synergistic effect with carbon coating and thereby greatly improved the rate capability of LiFePO₄. The 1 mol% Zr-doped LiFePO₄/C exhibited excellent rate capability with 125 mAh/g at 20 C and a stable capacity retention rate of 98.5% for 200 cycles at 5 C. Benefited from the contribution of Mg doping at Fe sites, Yan et al. [150] showed that 3% Mg-doped LiFePO₄/C composite possessed excellent rate and cycling performance, which exhibited a capacity drop rate of 0.02% per cycle during 1000 cycles at a high rate of 10 C (Fig. 5c). Besides cation doping, substitution of O₂[−] sites by anions such as F[−] and Cl[−] is also expected to effectively improve the electronic conductivity of LiFePO₄ [151]. Liu et al. [152] demonstrated that Cl[−] doping could change the microstructure of LiFePO₄, stabilize its structure and enhance its rate

capability, cycling performance and ion diffusion rate. Moreover, the Cl-doped LiFePO₄/C delivered a reversible capacity of 105.3 mAh/g with capacity retention of 91.5% after 500 cycles at 10 C, which is much higher than that of undoped LiFePO₄/C (62.7%).

Obviously, the Li⁺ ion diffusion distance of LiFePO₄ can be controlled by modifying the morphology, mainly by reducing the particle size and adjusting the directional growth of crystal planes [153]. Due to the shortened diffusion length, nano-sized LiFePO₄ particles show better electrochemical performance than micro-sized/bulk particles in terms of rate capability [154]. Alsamet et al. [155] synthesized nanoscale LiFePO₄ with plate-like morphology by a consecutive combination of sol-gel and hydrothermal methods. The as-prepared LiFePO₄ cathode delivered capacities of 126 mAh/g at 0.2 C and 70 mAh/g at 3 C, and exhibited stable charge/discharge cycling capability (capacity retention >97.5% after 100 cycles at 0.5 C). Unfortunately, decreasing particle size results in low tap density and low volumetric energy density, and high surface area intensifies undesired electrode-electrolyte interface reactions, leading to poor cycling performance [156]. Due to the anisotropy of the crystal structure, different crystal faces play different roles in the transport of Li⁺ ions. Li⁺ ions in LiFePO₄ tend to diffuse along the (010) plane, and exposing the crystal plane is expected to improve the rate capability of LiFePO₄ batteries [157]. However, the (010) facet tends to disappear during synthesis due to the high-energy surface of the crystal plane. To solve this problem, Pei et al. [158] used sodium dodecylbenzenesulfonate (SDBS) to adjust the morphology of particles to nanoparticles, nanorods and nanoplates by adsorbing on the surface of LiFePO₄ precursor with controllable *b*-axis thickness. Compared with nanoparticles (without SDBS), nanorods (0.0006 M SDBS), the obtained LiFePO₄/C nanoplates (0.003 M SDBS) showed an improved Li⁺ ion diffusion coefficient ($1.64 \times 10^{-11} \text{ cm}^2/\text{s}$), and delivered a discharge capacity of 162.9 mAh/g at 1 C and 107.9 mAh/g at 10 C (Fig. 5d and e). In order to meet the requirement of high tap density while maintaining all the advantages of nanomaterials, the material synthesis conditions are rationally optimized to generate ordered LiFePO₄ crystals with suitable morphological dimensions, which achieves a high degree of electrochemical reversibility while promoting

the rapid diffusion of Li^+ ions.

4.2. LiCoO_2 cathodes

Layered rock-salt structured LiCoO_2 was identified as cathode material for LIBs by Goodenough group in 1980 and was commercialized by Sony Corporation in 1991 [159]. LiCoO_2 crystal has a layered structure of $\alpha\text{-NaFeO}_2$ (rhombohedral space group R3-m) with alternating layers of LiO_2 and CoO_2 . Li and Co atoms are located at 3a and 3b sites, respectively, and arranged in alternating octahedral coordination on the (111) plane, while O atoms occupy site 6c with ccp stacking [160,161]. During the charging and discharging process, Li^+ ions in LiCoO_2 are intercalated/deintercalated, and the charge compensation is realized by $\text{Co}^{3+/4+}$ redox. The theoretical capacity of the LiCoO_2 is 274 mAh/g when all its Li^+ ions are removed. However, the deep delithiation of LiCoO_2 to higher voltages easily induces the oxidation of lattice oxygen, leading to severe structural deterioration and rapid decay in capacity as well as cyclability. Although direct Co-Co interaction and interconnected Li^+ ions in LiCoO_2 ensure good structural stability and high electronic conductivity ($\sim 1 \times 10^{-3}$ S/cm) and ionic conductivity (10^{-11} to 10^{-7} cm 2 /s), the main disadvantages of LiCoO_2 are poor thermal stability and low capacity [162,163].

Enormous research efforts have been done to elucidate the fundamental mechanisms of LiCoO_2 at high cutoff voltage to improve the capacity [164]. As shown in Fig. 6a, LiCoO_2 undergoes a gradual phase transition from H1 to H2, M1, H3, M2, and O1 phases, resulting in large anisotropic expansion and contraction along the *c*-axis and *a*-axis, respectively [165]. Specifically, the continuous removal of Li^+ ions from the Li_xCoO_2 lattice results in continuous changes of Li cations and Li vacancies in their spatial arrangement. Therefore, LiCoO_2 is structurally damaged due to its irreversible phase transition induced by high cut-off voltage, resulting in a rapid capacity decay. In order to improve the cyclic capacity and stability of LiCoO_2 , several strategies have been

considered to address the challenges associated with the high voltage applications [166]. Various methods, such as elemental doping and surface modification, have been widely used to improve the electrochemical performance of LiCoO_2 because of their ability to alter the physicochemical properties of cathode materials.

Elemental doping is an efficient solution to tune fundamental physical properties of materials, such as electronic conductivity, lattice parameters, and electrostatic energy by altering the lattice at the atomic level [167]. Many elements such as Mg, B, Al, Cr, and Ni have been used for doping, and their doping effect on the performance of LiCoO_2 at high voltages have been investigated [168]. Mg is considered as a good dopant in LiCoO_2 due to its nontoxicity and cheapness. Tukamoto et al. [162] first reported that Mg substitution reduced the initial discharge capacity of LiCoO_2 , but it improved the cycling performance at high voltage (4.3 V), which was subsequently confirmed by other authors. Huang et al. [169] proposed that Mg^{2+} ions could act as pillars in LiCoO_2 to effectively suppress unfavorable phase transitions and improve structural stability during lithiation/delithiation. As shown in Fig. 6b–e, the Mg-doped LiCoO_2 (LCO) in the form of $\text{Li}_{0.9}\text{Mg}_{0.05}\text{CoO}_2$ (LMCO) exhibits predominantly O3 phase behavior when charged to high voltages above 4.55 V, which is quite different from the undoped samples showing the M2 phase. Moreover, the undoped LiCoO_2 undergoes a larger volume change, resulting in severe structural degradation during long cycling, manifested by obvious cracks inside the LiCoO_2 grains (Fig. 6f and g). In addition, Al doping has been reported to decrease the electrostatic energy of LiCoO_2 and increase the intercalation voltage. Ceder's group observed experimentally for the first time that Al substitution in LiCoO_2 achieved a higher Li intercalation voltage than bare LiCoO_2 [170]. Some researchers have also investigated the synergistic effect of multi-elements co-substitution in LiCoO_2 on the electrochemical performance at high cut-off voltages [171–173]. Kong et al. [174] investigated the effect of Mg and F co-doping in the LiCoO_2 lattice structure, where Mg could act as a “pillar” in the lattice to provide stable

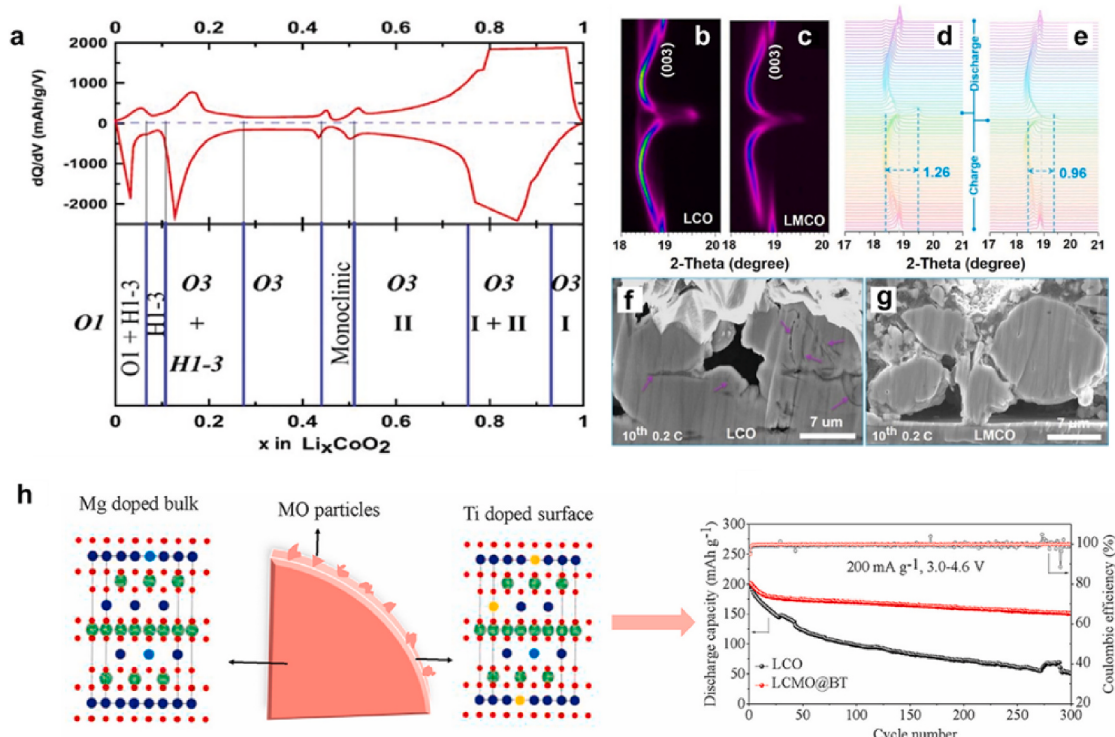


Fig. 6. (a) The structure evolution of LiCoO_2 with different delithiation [165]. (b–g) The (003) peak evolution of LCO (b) and LMCO (c) for the first cycle at 0.1 C, and their corresponding XRD patterns of LCO (d) and LMCO (e), cross-section SEM images of LCO (f) and LMCO (g) after 10 cycles at 0.2 C [169]. (h) Schematic illustration of the structure design strategy of LCMO@BT with MO (BaTiO_3 and TiO_2) particles dot coating, Ti surface doping and Mg bulk doping, and the cycling performance of LCO and LCMO@BT electrodes in the voltage between 3.0 and 4.6 V (vs. Li/Li^+) at a current density of 200 mA/g [183].

and locally extended channels for rapid transport of Li^+ ions, while F helped to stabilize oxygen redox due to the highest electronegativity, which greatly improved the cycling stability of LiCoO_2 .

LiCoO_2 will suffer from surface degradation/phase transition when it contacts with the electrolyte at high voltage during repeated charge/discharge. Hu et al. [175] investigated the cumulative effect of long-term fast charging at 6 C on 1.6 Ah LiCoO_2 /graphite pouch cells. Long-term fast charging accelerates Li inventory loss, and postmortem analysis reveals that surface structure, charge transfer resistance and Li-ion diffusion coefficient of the cathode degenerate during repeated fast charging, causing a large increase in polarization. Hence, surface engineering of high-voltage LiCoO_2 by introducing a protective layer can provide a direct effect to stabilize the surface structure for extending battery cycle life [176]. A variety of electrochemically inert coating materials have been used, typically including metal oxides, metal fluorides, and metal phosphates [177–181]. For example, Al_2O_3 , widely used as a coating material for LiCoO_2 surface protection, can greatly reduce electrolyte decomposition and irreversible side reactions, thus improving the cycle performance of cathode materials. Zhou et al. [182] reported a low-cost and environmentally friendly wet-chemical method for coating Al_2O_3 on LiCoO_2 using only aluminum sulfate and water as raw materials. The oxide coating can alleviate electrolyte decomposition and reduce the generation of irreversible solid electrolyte interface (SEI) components ($\text{LiF}/\text{Li}_2\text{CO}_3$ and organics), so the modified LiCoO_2 electrode exhibits excellent cycling stability (82.6% capacity retention after 500 cycles at 1 C) and competitive rate capability (130 mAh/g at 10 C). Furthermore, the structural stabilization of high-voltage LiCoO_2 can be synergistically promoted by a comprehensive strategy of bulk doping and surface coating. Hu et al. [183] proposed a multifunctional self-stabilizing modification strategy including trace Mg bulk doping, surface-gradient Ti doping, and BaTiO_3 dot coating in LiCoO_2 . By using advanced characterization techniques, it was clearly revealed that Mg^{2+} doping can alter the oxygen stacking behavior, thereby reducing the phase transition from O_3 to H1-3 and structural damage; Ti surface gradient doping can enhance the structural stiffness of the particles while significantly inhibits irreversible oxygen redox under high voltage; and BaTiO_3 can also stabilize the electrode/electrolyte interface. These advantages simultaneously promote the ultra-stable cycling of the LiCoO_2 at 4.6 V, achieving an excellent capacity retention of about 75.0% at 200 mA/g after 300 cycles, as shown in Fig. 6h.

4.3. Multi-layered cathodes

Multi-layered cathodes have been paid much attention due to their good overall performance, low cost and high energy density since they can overcome the shortcomings of the individual layered materials [184]. Compared with LFP, multi-layered cathodes are more suitable for high-rate batteries due to their better conductivity, especially at low temperature. Multi-layered material typically contains Ni, Co, Mn or Al elements, with hexagonal $\alpha\text{-NaFeO}_2$ (R3-m) structure and repeating O_3 structures, in which edge-sharing LiO_6 and TMO_6 octahedra occupy alternating atomic layers, Li occupies the 3b site and TM occupies the 3a site [185]. Typically, utilizing $\text{Ni}^{2+}/\text{Ni}^{3+}/\text{Ni}^{4+}$ redox to enable materials to achieve high capacity, the presence of Co inhibits cation mixing, while Mn or Al helps to stabilize the structure, which drives the research community and industry to increase the proportion of Ni in pursuit of higher energy density. Unfortunately, materials with high Ni content face some difficulties in commercialization. The increase of Ni content leads to a series of problems such as weakened structural stability, microcracks, intensified side reactions, and gas evolution, resulting in decreased battery life and safety [186]. Yang et al. [187] systematically explored the Ni-included cathodes (NMC532, 622, and 811) paired with graphite and cycled under 6 C condition. The cathode crack density increased with Ni content, as a result, large particle size and great anisotropic volume change, and non-uniform surface degradation with rock-salt formation were observed due to SOC heterogeneity in the

cathode. Therefore, it is necessary to address the structural and chemical instabilities associated with increasing Ni content to construct highly stable Ni-rich cathode materials to improve their thermal stability and increase practical capacity.

Replacing Li sites, TM sites, or O sites with extrinsic ions as dopants is considered to be a simple, effective and widely adopted strategy to improve the electrochemical performance and structural stability of materials [122,188]. Experiments and theoretical calculations show that Mg^{2+} ions tend to preferentially occupy the Li layer and act as pillars due to its similar ionic radius (0.72 Å) to Li, suppressing the phase transition and alleviating the anisotropic lattice distortion during cycling. The presence of Mg^{2+} ions in Li slabs helps to counteract electrostatic repulsion between adjacent oxygen layers through Mg–O electrostatic attraction, thereby slowing the change of lattice parameter c and suppressing the formation of the H3 phase on deep delithiation states [189, 190]. Gomez-Martin et al. [191] systematically studied the impact of Mg doping in $\text{LiNi}_{0.90}\text{Mn}_{0.05}\text{Co}_{0.05}\text{O}_2$ on the performances of full cells with graphite anode under practical testing conditions. The addition of 1–1.5 mol% Mg^{2+} improved the structural stability and capacity retention without reducing the capacity and energy density at the material level. However, it is worth noting that the use of one dopant does not solve all the problems of multi-layered cathode materials, and understanding the influence mechanism of each dopant and the synergistic mitigation of its side effects by co-doping is crucial to improve the overall performance [192,193]. Cui et al. [194] reported an exceptionally stable cycling of $\text{LiNi}_{0.885}\text{Co}_{0.100}\text{Al}_{0.015}\text{O}_2$ by introducing 0.3 mol% Zr and 1.5 mol% B into the $\text{LiNi}_{0.885}\text{Co}_{0.100}\text{Al}_{0.015}\text{O}_2$ cathode. The two dopants are combined to achieve a synergistic effect as each dopant separately modifies the cathode structure at the atomic and micro-scale levels, where Zr ions stabilize the delithiated structure through a “pillar effect”, while B modifies the cathode microstructure to a configuration that is conducive to dissipating the detrimental anisotropic strain energy. As a result, Zr- and B-doped $\text{LiNi}_{0.885}\text{Co}_{0.100}\text{Al}_{0.015}\text{O}_2$ (denoted as Zr0.3&B1.5-NCA89) can significantly suppress the formation of microcracks and exhibit a remarkable 95% capacity retention after 1000 cycles (Fig. 7a).

Uniform extrinsic coating on the surface of cathode materials can reduce interfacial side reactions, such as moisture intrusion, TM dissolution, gas evolution, and mechanical cracking, and has been widely used to improve the electrochemical performance and thermal stability of cathodes [197]. Currently, many coating materials such as oxides, fluorides, phosphates, lithium-ion conductors, and other conductive coatings have been used to protect cathode materials by varying the primary particle level and secondary particle level [198,199]. Oxides such as ZrO_2 , TiO_2 , and Al_2O_3 , are commonly used as physical protective barriers to protect the materials from electrolyte corrosion. Zhao et al. [195] obtained precise Al_2O_3 coating on $\text{LiNi}_{0.5}\text{Co}_{0.2}\text{Mn}_{0.3}\text{O}_2$ surface via atomic layer deposition (ALD), which not only prevented the shuttle effect of dissolved transition metal ions, but also reduced the internal stress variation of the particles, showing good electrochemical stability during charging and discharging process (Fig. 7b). Considering the poor ionic and electronic conductivities of most inactive coating materials, ionic/electronic conducting materials as coatings can not only protect the cathode interface but also improve $\text{Li}^+/\text{electron}$ transfer between cathode particles, which is helpful for fast charging [200,201]. Yan et al. [202] reported that infusing Li_3PO_4 into the grain boundaries of $\text{LiNi}_{0.76}\text{Mn}_{0.14}\text{Co}_{0.10}\text{O}_2$ secondary particles brought fast channels for Li^+ ion transport, and prevented the liquid electrolyte from infiltrating the boundary, which significantly improved the capacity retention and voltage stability. Although the above modification strategies can improve the structural stability of cathode, it is difficult to control the origin of the volume expansion/contraction inside the material. In NMC cathode materials, high-content Ni ions increase the capacity but introduce cationic mixing and phase transition, Mn ions stabilize the structure, and Co ions are usually incorporated to suppress cationic mixing and also contribute to the capacity. Therefore, compositionally tailored cathodes, mainly including core-shell, concentration-gradient

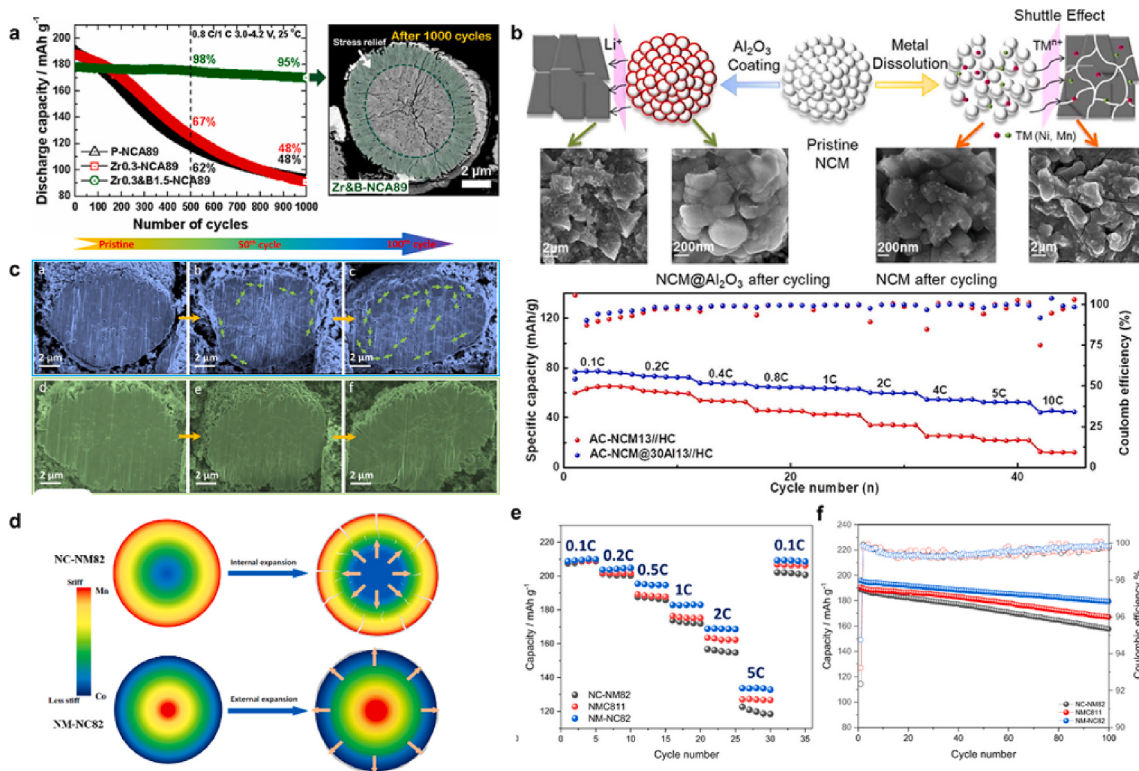


Fig. 7. (a) Electrochemical performance of P-NCA89, Zr0.3-NCA89, B1.5-NCA89, and Zr0.3&B1.5-NCA89, and cross-sectional SEM images of Zr0.3&B1.5-NCA89 after 1000 cycles [194]. (b) Schematic representation of the changes in the cathodes and the corresponding SEM images after 200 cycles, as well as rate capability of LiNi_{0.5}Co_{0.2}Mn_{0.3}O₂@Al₂O₃ and LiNi_{0.5}Co_{0.2}Mn_{0.3}O₂, respectively [195]. (c) Cross-sectional images of pristine NC-NM82 particle (blue) and NM-NC82 particle (green) after 50, and 100 cycles. (d) The mechanism schematic of two different concentration gradient designs and their mechanical stability. (e) Rate capability of the NC-NM82, NMC811, and NM-NC82. (f) Cycling performance of the NC-NM82, NMC811, and NM-NC82 at a current rate of C/2 within a voltage range of 2.8–4.4 V after three activation cycles [196]. (For interpretation of the references to colour in this figure legend, the reader is referred to the Web version of this article.)

core-shell, and full concentration gradient, were introduced to meet the requirements of high capacity and enhanced safety of electrode materials [203,204]. Liu et al. [196] thoroughly investigated the effects of Co-rich and Mn-rich surfaces on the mechanical properties of Ni-rich materials using ex-situ and in-situ characterizations, and found that the Co-rich surface exhibited better rate capability and cycling performance, while the Mn-rich surface showed severe grain cracking caused by internal tensile stress, which gave a new design principle for concentration gradient cathodes (Fig. 7c–f).

5. Electrolyte

High-performance cathode and anode electrode materials and corresponding non-aqueous electrolyte systems are the intrinsic factors for achieving high performances including rate capability of LIBs [205]. The electrolyte is called the “blood” of the battery, acts as the bridge to connect the cathode and anode, and plays the function of ion conduction inside the battery. It can not only regulate the electrode/electrolyte interface, but also affect the performances of the battery, mainly including capacity, internal resistance, rate charge-discharge performance, operating temperature, and safety performance [206]. Currently, the electrolytes used in LIBs are LiPF₆ salts dissolved in carbonate-based solvent mixtures with little variation in salt concentration, solvent ratio, and functional additives. Briefly, the electrolyte working process includes the migration of solvated Li⁺ ions and the desolvation of solvated Li⁺ ions at the electrode/electrolyte interface. Usually, the diffusion coefficient of Li⁺ ions in liquid electrolytes is several orders of magnitude higher than in solid electrodes, so the desolvation of solvated Li⁺ ions at the electrode/electrolyte interface will be a more important factor in determining the fast-charging ability of

battery.

In most cases, increasing the ionic conductivity of the electrolyte is beneficial for reducing solvation and desolvation activation energies of Li⁺ ions, which is favorable for fast charging [207]. Demonstrated by Gao et al., the combination of low-molecular-weight solvents can extend the useful conductivity and hence reduce concentration polarization, which is key to fast-charging electrolytes [208]. However, the importance of Li⁺ ions solvation and desolvation in determining the rate performance of batteries should not be overlooked. The structure and stability of the Li⁺ ion solvation shell in the electrolyte is affected by the type and ratio of solvent molecules in the inner shell and counter anion in the outer shell, as shown in Fig. 8a [10,209]. Yao et al. [210] reported a novel weakly solvated electrolyte (WSE) composed of pure non-polar solvents, revealing that the interfacial chemistry was controlled by competitive coordination between anions and solvents with lithium ions based on first-principles calculations, and that the anion-derived SEI exhibited superior interfacial charge transport kinetics and high stability, enabling fast charging and long-term cycling of graphite anode. Incorporating multiple solvents and multiple lithium salts into the electrolyte is a simple and effective method to alter the structure and stability of the solvation shell of Li⁺ ions [211–214]. Amanchuku et al. [215] introduced a new concept of using non-reactive and non-polar alkane co-solvents in the electrolytes and experimentally demonstrated the importance of controlling ionic solvation. The addition of small-molecule alkanes to ether solvents containing lithium salts changes the Li⁺ ions solvation structure in the electrolyte, reducing the solvation free energy, and hence lowering the nucleation and growth overpotentials required for Li deposition and exfoliation. As shown in Fig. 8b and c, incorporation of non-reactive additives hexane (Hx) into 0.1 M lithium bis(trifluoromethane)sulfonimide (LiTFSI) dissolved in 1,

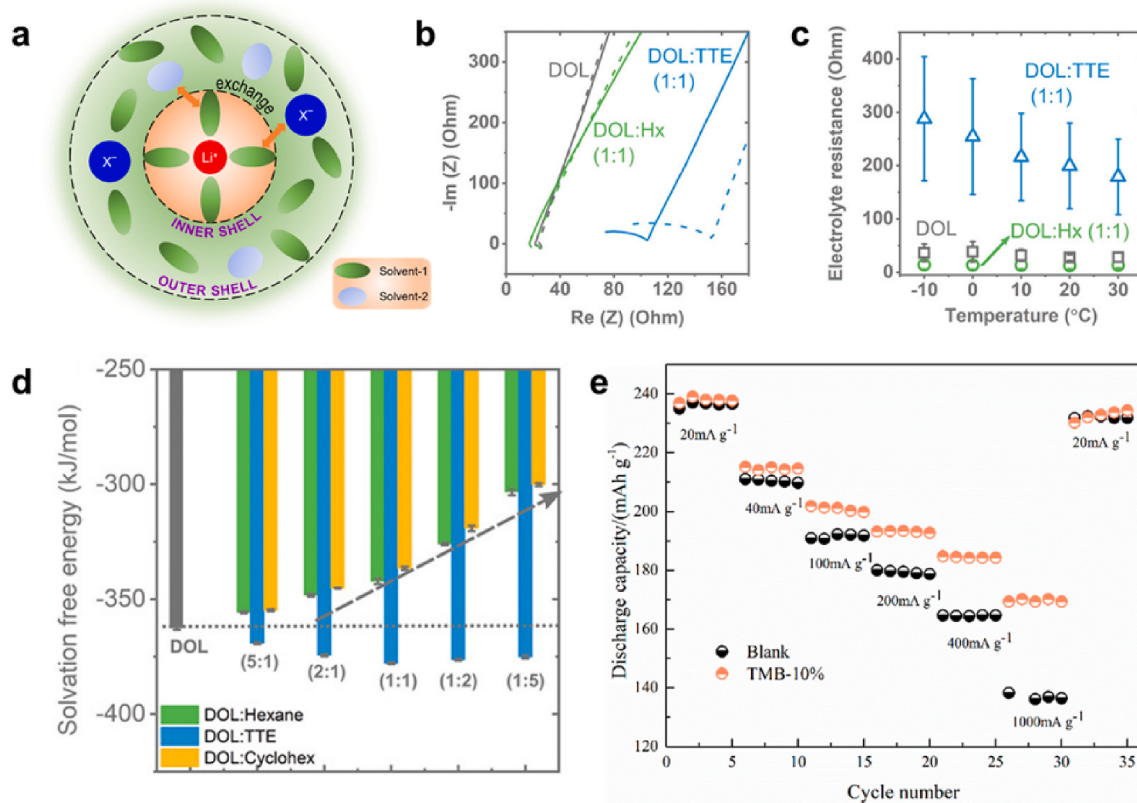


Fig. 8. (a) Schematic illustration of the structure and stability of Li⁺ ion solvation shell in the mixture of solvent-1 and solvent-2, showing that the Li⁺-coordinated solvent molecules in the inner shell dynamically exchange with the solvent molecules and counter anions (X⁻) in the outer shell [10]. (b-d) EIS Nyquist plots of the electrolyte mixtures at 30 °C (bold) and 0 °C (dashed) (b), total electrolyte resistance (contact + bulk resistance) as a function of temperature (c), and computed lithium-ion solvation free energies in different electrolyte mixtures (d) [215]. (e) Rate performance of LiNi_{0.88}Co_{0.09}Al_{0.03}O₂ in blank and 10% TMB-containing electrolytes (1 C = 200 mA/g) [224].

3-dioxolane (DOL) resulted in lower electrolyte resistance than reactive fluorinated additive 1,1,2,2-tetrafluoroethyl 2,2,3,3-tetrafluoropropylether (TTE), and its corresponding solvation ability was weak based on molecular dynamics (MD) simulation. The “solvation effect” is illustrated in Fig. 8d.

Instability at the electrode/electrolyte interface is another major reason for electrolyte depletion, loss of cyclable lithium ions and limitation of charge transfer across electrode-electrolyte interfaces during fast charging. Electrolyte decomposition often occurs in lithiation electrode under battery operating conditions, which can significantly affect battery cycling and rate performance [216]. Yao et al. demonstrated that the enhanced charge transfer kinetics led to better fast-charging performance, even with a 40% drop in electrolyte ionic conductivity [217]. Furthermore, the dissolved transition metal ions as well as soluble byproducts generated at electrode side crossover between cathode and anode result in severe deterioration of the electrode surface. Therefore, designing a stable and robust electrode/electrolyte interface can undoubtedly reduce the side reaction between the electrolyte and cathode, so as to exert great influence on the overall electrochemical performance of battery, including the rate capability. Electrolyte additives can effectively tailor the electrochemical properties of electrolytes as well as electrode/electrolyte interphase. The electrolyte developed by Yang et al. achieved smooth desolvation and high ionic conductivity at low temperature by utilizing the weak solvation molecule ethyl trifluoroacetate and film-forming fluoroethylene carbonate [218]. The synergistic effect of the tamed electrolyte and optimized SEI enabled the graphite to exhibit a reversible charge/discharge capacity of 183 mAh/g at -30 °C and to be rapidly charged under 6 C at room temperature. Liang et al. [219] proposed flame-retardant electrolyte with retentive

solvation configuration and relatively weakened anion-coordination and non-solvating fluorinated, exhibiting prolonged cyclability up to 1400 cycles with an excellent capacity retention of as high as 92.4%. Similarly, some novel electrolytes such as ionic liquids (ILs) can participate in the formation of stable solid-state interfacial films, and adjust the sheath structure of Li⁺ solvation to accelerate the kinetics of Li ions [220]. The additives with oxygen-containing groups such as S–O, B–O and P–O are found to contribute to the ionic conductivity of the cathode/electrolyte interface (CEI), possibly because the oxygen anions in these groups provide paths for easy transportation of Li⁺ ions [221–223]. Xiao et al. [224] demonstrated that a 10% trimethyl borate (TMB)-containing electrolyte formed a more stable and conductive CEI film on the surface of the LiNi_{0.88}Co_{0.09}Al_{0.03}O₂ cathode, which not only prevented the decomposition of the electrolyte, but also suppressed the structural degradation of the bulk phase and significantly improved the cycling and rate capability (Fig. 8e). Besides, extensive researches have been conducted on exploring novel lithium salts like lithium tetrafluoroborate (LiBF₄), lithium bis(fluorosulfonyl)imide (LiFSI) and lithium nitrate (LiNO₃) as functional additives [225–227]. The CEI film generated by inorganic film-forming additives is more ionically conductive than the CEI generated by decomposition of organic additives, which is beneficial to improve the capacity retention and rate capability of the electrode. In addition, some flame retardant additives or solid electrolyte can be used to reduce the flammability of the electrolyte and reduce the side reactions at the interface, thereby improving the safety of the battery [228,229]. Zou et al. [230] designed a new fluorine-contained carboxylate-based electrolyte, which could not only show flame retardancy but also regulate the Li⁺ solvation structure by the solvent-solvent interaction (van der Waals force or intermolecular

interaction), thus achieving high-power capability up to 5 C for the full cell of graphite||LiNi_{0.8}Co_{0.1}Mn_{0.1}O₂.

6. Conclusions

The development of fast charging materials is the key to realize fast-charging LIBs. The main limiting factors associated with LIBs fast charging can be attributed to charge transfer and mass transport issues. The charge transfer involves the solvation/desolvation of Li⁺ ions and their diffusion across the solid-electrolyte interfacial films, while mass transport refers to the transport of Li⁺ ions in the electrolyte and within the electrode materials. Addressing the above issues can alleviate/reduce the problems such as low material utilization, lithium deposition, and electrolyte/electrode side reactions encountered in the batteries during fast charging. This review provides an overview of the current state of electrode and electrolyte materials for fast charging, with a focus on how to facilitate Li⁺ ion diffusion kinetics and mass transport in electrode materials. We summarize the current status of cathode and anode materials for fast charging of LIBs, and focus on the strategies to promote Li⁺ ions diffusion kinetics or structural stability of materials, such as structural design, morphology modulation, surface/interface modification. The strategies to use multiple solvents, lithium salts, and additives to alter the solvation/desolvation activation energies of Li⁺ ions or to form stable interfacial phases (SEI and CEI) at the electrode/electrolyte are also discussed.

In addition to electrode and electrolyte materials design, battery engineering is equally important for improving fast-charging capability, longevity, and safety. The fast-charging capability can also be optimized by adjusting parameters such as electrode composition, thickness and porosity, and positive and negative electrode capacity ratio (N/P ratio). The electrode architecture is an important factor to affect the high-rate performance of batteries because it directly or indirectly affects the electrode resistance and the charge-discharge depth of batteries. Since the utilization rate of active materials gradually decreases during fast charging, the N/P ratio design cannot be ignored, which can avoid dangerous Li electroplating during battery operation. Although good development in fast-charging electrode materials has been achieved for both academy and industry, there are still many challenges that need to be further addressed. With further research and development, we believe that some new breakthroughs in advanced fast-charging technologies will come forth for rechargeable batteries to better solve the “range anxiety” of EVs in a near future.

Declaration of competing interest

The authors declare that they have no known competing financial interests or personal relationships that could have appeared to influence the work reported in this paper.

Data availability

No data was used for the research described in the article.

Acknowledgement

This work was supported by the National Natural Science Foundation of China (Grant Nos. 5202780089 & 52202283).

References

- [1] Y. Huang, A. Manthiram, *Adv. Energy Mater.* 11 (2021), 2002817.
- [2] W. Li, E.M. Erickson, A. Manthiram, *Nat. Energy* 5 (2020) 26–34.
- [3] X. Wang, Y. Yang, J. Guo, Z. Gu, E.H. Ang, Z. Sun, W. Li, H. Liang, X. Wu, *J. Mater. Sci. Technol.* 102 (2022) 72–79.
- [4] Q. Huang, S. Ni, M. Jiao, X. Zhong, G. Zhou, H.M. Cheng, *Small* 17 (2021), 2007676.
- [5] X. Lin, K. Khosravinia, X. Hu, J. Li, W. Lu, *Prog. Energ. Combust.* 87 (2021), 100953.
- [6] S. Li, K. Wang, G. Zhang, S. Li, Y. Xu, X. Zhang, X. Zhang, S. Zheng, X. Sun, Y. Ma, *Adv. Funct. Mater.* 32 (2022), 2200796.
- [7] W. Cai, Y. Yao, G. Zhu, C. Yan, L. Jiang, C. He, J. Huang, Q. Zhang, *Chem. Soc. Rev.* 49 (2020) 3806–3833.
- [8] M. Li, M. Feng, D. Luo, Z. Chen, *Cell Reports Physical Science* (2020), 100212.
- [9] S. Wan, W. Ma, Y. Xiao, S. Chen, *Batteries & Supercaps* 5 (2022), 202200368.
- [10] S.S. Zhang, *Info* 3 (2021) 125–130.
- [11] G.L. Zhu, C.Z. Zhao, J.Q. Huang, C. He, J. Zhang, S. Chen, L. Xu, H. Yuan, Q. Zhang, *Small* 15 (2019), 1805389.
- [12] M. Weiss, R. Ruess, J. Kasnatscheew, Y. Levartovsky, N.R. Levy, P. Minnmann, L. Stoltz, T. Waldmann, M. Wohlfahrt Mehrens, D. Aurbach, M. Winter, Y. Ein Eli, J. Janek, *Adv. Energy Mater.* (2021), 2101126.
- [13] P.F. Smith, K.J. Takeuchi, A.C. Marschilok, E.S. Takeuchi, *Accounts Chem. Res.* 50 (2017) 544–548.
- [14] N. Wassiliadis, J. Schneider, A. Frank, L. Wildfeuer, X. Lin, A. Jossen, M. Lienkamp, *J. Energy Storage* 44 (2021), 103306.
- [15] Q. An, X. Sun, J. Guo, S. Cai, C. Zheng, *J. Electrochem. Soc.* 167 (2020), 140528.
- [16] R. Yazami, P. Touzain, *J. Power Sources* 9 (1983) 365–371.
- [17] A.S. Ho, D.Y. Parkinson, D.P. Finegan, S.E. Trask, A.N. Jansen, W. Tong, N. P. Balsara, *ACS Nano* 15 (2021) 10480–10487.
- [18] Z.M. Konz, B.M. Wirtz, A. Verma, T. Huang, H.K. Bergstrom, M.J. Crafton, D. E. Brown, E.J. McShane, A.M. Colclasure, B.D. McCloskey, *Nat. Energy* (2023) 1–12.
- [19] Y. Li, X. Feng, D. Ren, M. Ouyang, L. Lu, X. Han, *ACS Appl. Mater. Interfaces* 11 (2019) 46839–46850.
- [20] J. Hu, S. Zhong, T. Yan, *J. Power Sources* 508 (2021), 230342.
- [21] J. Kim, H.I. Cho, Y.S. Cho, S.H. Lee, C.R. Park, *Carbon* 203 (2023) 152–160.
- [22] Y. Wu, W. Wang, J. Ming, M. Li, L. Xie, X. He, J. Wang, S. Liang, Y. Wu, *Adv. Funct. Mater.* 29 (2019), 1805978.
- [23] S. Yan, X. Chen, P. Zhou, P. Wang, H. Zhou, W. Zhang, Y. Xia, K. Liu, *J. Energy Chem.* 67 (2022) 467–473.
- [24] W. Cai, C. Yan, Y. Yao, L. Xu, R. Xu, L. Jiang, J. Huang, Q. Zhang, *Small Structures* 1 (2020), 2000010.
- [25] S. Thinius, M.M. Islam, P. Heijmans, T. Bredow, *J. Phys. Chem. C* 118 (2014) 2273–2280.
- [26] F. Yao, F. Güneş, H.Q. Ta, S.M. Lee, S.J. Chae, K.Y. Sheem, C.S. Cojocaru, S.S. Xie, Y.H. Lee, *J. Am. Chem. Soc.* 134 (2012) 8646–8654.
- [27] Q. Cheng, R. Yuge, K. Nakahara, N. Tamura, S. Miyamoto, *J. Power Sources* 284 (2015) 258–263.
- [28] S. Lim, J. Kim, Y. Yamada, H. Munakata, Y. Lee, S. Kim, K. Kanamura, *J. Power Sources* 355 (2017) 164–170.
- [29] J. Billaud, F. Bouville, T. Magrini, C. Villevieille, A.R. Studart, *Nat. Energy* 1 (2016) 1–6.
- [30] D.W. Guo, X.R. Zeng, F. Deng, J.Z. Zou, H.C. Sheng, *N. Carbon Mater.* 30 (2015) 419–424.
- [31] E.G. Leggesse, C. Chen, J. Jiang, *Carbon* 103 (2016) 209–216.
- [32] T. Kim, E.K. Jeon, Y. Ko, B.Y. Jang, B. Kim, H. Song, *J. Mater. Chem. 2* (2014) 7600–7605.
- [33] P. Du, B. Zhang, L. Cao, X. Ou, *Chem. Commun.* 58 (2022) 7372–7375.
- [34] S. Dong, Y. Song, K. Ye, J. Yan, G. Wang, K. Zhu, D. Cao, *EcoMat* 4 (2022), 12212.
- [35] N. Yao, F. Liu, Y. Zou, H. Wang, M. Zhang, X. Tang, Z. Wang, M. Bai, T. Liu, W. Zhao, R. Xue, Y. Liu, Y. Ma, *Energy Storage Mater.* 55 (2023) 417–425.
- [36] D. Chen, W. Zhang, K. Luo, Y. Song, Y. Zhong, Y. Liu, G. Wang, B. Zhong, Z. Wu, X. Guo, *Energy Environ. Sci.* 14 (2021) 2244–2262.
- [37] D. Saurel, J. Segalini, M. Jauregui, A. Pendashiteh, B. Daffos, P. Simon, M. Casabanas, *Energy Storage Mater.* 21 (2019) 162–173.
- [38] Y. Liu, Y.X. Lu, Y.S. Xu, Q.S. Meng, J.C. Gao, Y.G. Sun, Y.S. Hu, B.B. Chang, C. T. Liu, A.M. Cao, *Adv. Mater.* 32 (2020), 2000505.
- [39] G. Yang, X. Li, Z. Guan, Y. Tong, B. Xu, X. Wang, Z. Wang, L. Chen, *Nano Lett.* 20 (2020) 3836–3843.
- [40] L. Zhang, W.A. Wang, S. Lu, Y. Xiang, *Adv. Energy Mater.* 11 (2021), 2003640.
- [41] L. Xie, C. Tang, Z. Bi, M. Song, Y. Fan, C. Yan, X. Li, F. Su, Q. Zhang, C. Chen, *Adv. Energy Mater.* 11 (2021), 2101650.
- [42] G. Wang, M. Yu, X. Feng, *Chem. Soc. Rev.* 5 (2021) 2388–2443.
- [43] S. Alvin, H.S. Cahyadi, J. Hwang, W. Chang, S.K. Kwak, J. Kim, *Adv. Energy Mater.* 10 (2020), 2000283.
- [44] P. Liu, Y. Li, Y. Hu, H. Li, L. Chen, X. Huang, *J. Mater. Chem. 4* (2016) 13046–13052.
- [45] J. Ni, Y. Huang, L. Gao, *J. Power Sources* 223 (2013) 306–311.
- [46] L. Qie, W. Chen, Z. Wang, Q. Shao, X. Li, L. Yuan, X. Hu, W. Zhang, Y. Huang, *Adv. Mater.* 24 (2012) 2047–2050.
- [47] J. Wang, Y. Xia, Y. Liu, W. Li, D. Zhao, *Energy Storage Mater.* 22 (2019) 147–153.
- [48] Y. Du, G. Sun, Y. Li, J. Cheng, J. Chen, G. Song, Q. Kong, L. Xie, C. Chen, *Carbon* 178 (2021) 243–255.
- [49] M. Li, Z. Bi, L. Xie, G. Sun, Z. Liu, Q. Kong, X. Wei, C. Chen, *ACS Sustain. Chem. Eng.* 7 (2019) 14796–14804.
- [50] W. Li, M. Chen, C. Wang, *Mater. Lett.* 65 (2011) 3368–3370.
- [51] P. Du, X. Fan, B. Zhang, L. Cao, J. Ren, X. Ou, X. Guo, Q. Liu, *Energy Storage Mater.* 50 (2022) 648–657.
- [52] H. Geng, Y. Peng, L. Qu, H. Zhang, M. Wu, *Adv. Energy Mater.* 10 (2020), 1903030.
- [53] H. Sun, Y. Zhang, J. Zhang, X. Sun, H. Peng, *Nat. Rev. Mater.* 2 (2017) 1–12.
- [54] Y. Yu, H. Zhang, X. Yang, J. Gou, X. Tong, X. Li, H. Zhang, *Energy Storage Mater.* 19 (2019) 88–93.

- [55] X.Y. Yang, L.H. Chen, Y. Li, J.C. Rooke, C. Sanchez, B.L. Su, *Chem. Soc. Rev.* **46** (2017) 481–558.
- [56] F. Holtstiege, T. Koç, T. Hundehege, V. Siozios, M. Winter, T. Placke, *ACS Appl. Energy Mater.* **1** (2018) 4321–4331.
- [57] S. Lou, Y. Zhao, J. Wang, G. Yin, C. Du, X. Sun, *Small* **15** (2019), 1904740.
- [58] M. Vijayakumar, S. Kerisit, K.M. Rosso, S.D. Burton, J.A. Sears, Z. Yang, G. L. Graff, J. Liu, J. Hu, *J. Power Sources* **196** (2011) 2211–2220.
- [59] H. Zhang, Y. Yang, H. Xu, L. Wang, X. Lu, X. He, *Info* **4** (2022), 12228.
- [60] D. Ahn, X. Xiao, *Electrochim. Commun.* **13** (2011) 796–799.
- [61] I. Belharouak, G.M. Koenig, K. Amine, *J. Power Sources* **196** (2011) 10344–10350.
- [62] B. Zhao, R. Ran, M. Liu, Z. Shao, *Mater. Sci. Eng. R Rep.* **98** (2015) 1–71.
- [63] G. Zhu, Y. Wang, Y. Xia, *Energy Environ. Sci.* **5** (2012) 6652–6667.
- [64] J. Li, S. Hwang, F. Guo, S. Li, Z. Chen, R. Kou, K. Sun, C. Sun, H. Gan, A. Yu, E. A. Stach, H. Zhou, D. Su, *Nat. Commun.* **10** (2019).
- [65] V. Aravindan, Y. Lee, R. Yazami, S. Madhavi, *Mater. Today* **18** (2015) 345–351.
- [66] Y. He, B. Li, M. Liu, C. Zhang, W. Lv, C. Yang, J. Li, H. Du, B. Zhang, Q. Yang, J. Kim, F. Kang, *Sci. Rep.* **2** (2012) 913.
- [67] T. Yuan, Z. Tan, C. Ma, J. Yang, Z. Ma, S. Zheng, *Adv. Energy Mater.* **7** (2017), 1601625.
- [68] F. Bonaccorso, L. Colombo, G. Yu, M. Stoller, V. Tozzini, A.C. Ferrari, R.S. Ruoff, V. Pellegrini, *Science* **347** (2015), 1246501.
- [69] V. Chabot, D. Higgins, A. Yu, X. Xiao, Z. Chen, J. Zhang, *Energy Environ. Sci.* **7** (2014) 1564–1596.
- [70] Y. Tang, Y. Zhang, X. Rui, D. Qi, Y. Luo, W.R. Leow, S. Chen, J. Guo, J. Wei, W. Li, J. Deng, Y. Lai, B. Ma, X. Chen, *Adv. Mater.* **28** (2016) 1567–1576.
- [71] X. Meng, J. Liu, X. Li, M.N. Banis, J. Yang, R. Li, X. Sun, *RSC Adv.* **3** (2013) 7285.
- [72] J. Choi, W. Ryu, K. Park, J. Jo, S. Jo, D. Lim, I. Kim, *Sci. Rep.* **4** (2015) 7334.
- [73] L. Sun, W. Kong, H. Wu, Y. Wu, D. Wang, F. Zhao, K. Jiang, Q. Li, J. Wang, S. Fan, *Nanoscale* **8** (2016) 617–625.
- [74] C. Wang, S. Wang, Y. He, L. Tang, C. Han, C. Yang, M. Wagemaker, B. Li, Q. Yang, J. Kim, F. Kang, *Chem. Mater.* **27** (2015) 5647–5656.
- [75] X. Jia, Y. Kan, X. Zhu, G. Ning, Y. Lu, F. Wei, *Nano Energy* **10** (2014) 344–352.
- [76] C. Wang, S. Wang, L. Tang, Y. He, L. Gan, J. Li, H. Du, B. Li, Z. Lin, F. Kang, *Nano Energy* **21** (2016) 133–144.
- [77] W. Zhu, H. Yang, W. Zhang, H. Huang, X. Tao, Y. Xia, Y. Gan, X. Guo, *RSC Adv.* **5** (2015) 74774–74782.
- [78] C. Wang, X. Wan, L. Duan, P. Zeng, L. Liu, D. Guo, Y. Xia, A.A. Elzatahry, Y. Xia, W. Li, D. Zhao, *Angew. Chem. Int. Ed.* **58** (2019) 15863–15868.
- [79] H. Duan, J. Li, H. Du, S.W. Chiang, C. Xu, W. Duan, F. Kang, *J. Phys. Chem. C* **119** (2015) 5238–5245.
- [80] C.W. Xiao, Y. Ding, J.T. Zhang, X.Q. Su, G.R. Li, X.P. Gao, P.W. Shen, *J. Power Sources* **248** (2014) 323–329.
- [81] T. Yi, S. Yang, X. Li, J. Yao, Y. Zhu, R. Zhu, *J. Power Sources* **246** (2014) 505–511.
- [82] T. Subburaj, K. Prasanna, K.J. Kim, P.R. Ilango, Y.N. Jo, C.W. Lee, *J. Power Sources* **280** (2015) 23–29.
- [83] H. Cho, H. Son, D. Kim, M. Lee, S. Boateng, H. Han, K.M. Kim, S. Kim, H. Choi, T. Song, K.H. Lee, *J. Phys. Chem. C* **121** (2017) 14994–15001.
- [84] C. Yang, S. Yu, Y. Ma, C. Lin, Z. Xu, H. Zhao, S. Wu, P. Zheng, Z. Zhu, J. Li, N. Wang, *J. Power Sources* **360** (2017) 470–479.
- [85] S. Repp, E. Harputlu, S. Gurgen, M. Castellano, N. Kremer, N. Pompe, J. Wörner, A. Hoffmann, R. Thomann, F.M. Emen, S. Weber, K. Ocakoglu, E. Erdem, *Nanoscale* **10** (2018) 1877–1884.
- [86] H. Song, S. Yun, H. Chun, M. Kim, K.Y. Chung, H.S. Kim, B. Cho, Y. Kim, *Energy Environ. Sci.* **5** (2012) 9903.
- [87] Q. Zhang, M.G. Verde, J.K. Seo, X. Li, Y.S. Meng, *J. Power Sources* **280** (2015) 355–362.
- [88] Y. Bai, C. Gong, N. Lun, Y. Qi, *J. Mater. Chem. 1* (2013) 89–96.
- [89] G.B. Xu, L.W. Yang, X.L. Wei, J.W. Ding, J.X. Zhong, P.K. Chu, *J. Power Sources* **295** (2015) 305–313.
- [90] G. Du, N. Sharma, V.K. Peterson, J.A. Kimpton, D. Jia, Z. Guo, *Adv. Funct. Mater.* **21** (2011) 3990–3997.
- [91] Y. Ma, B. Ding, G. Ji, J.Y. Lee, *ACS Nano* **7** (2013) 10870–10878.
- [92] M. Ji, Y. Xu, Z. Zhao, H. Zhang, D. Liu, C. Zhao, X. Qian, C. Zhao, *J. Power Sources* **263** (2014) 296–303.
- [93] R. Wang, X. Cao, D. Zhao, L. Zhu, L. Xie, J. Li, Y. Miao, *ACS Appl. Mater. Interfaces* **12** (2020) 39170–39180.
- [94] D. Wang, H. Liu, Z. Shan, D. Xia, R. Na, H. Liu, B. Wang, J. Tian, *Energy Storage Mater.* **27** (2020) 387–395.
- [95] Z. Cao, P. Xu, H. Zhai, S. Du, J. Mandal, M. Dontigny, K. Zaghib, Y. Yang, *Nano Lett.* **16** (2016) 7235–7240.
- [96] S.C. Lee, S.M. Lee, J.W. Lee, J.B. Lee, S.M. Lee, S.S. Han, H.C. Lee, H.J. Kim, *J. Phys. Chem. C* **113** (2009) 18420–18423.
- [97] H. Xu, X. Hu, Y. Sun, W. Luo, C. Chen, Y. Liu, Y. Huang, *Nano Energy* **10** (2014) 163–171.
- [98] G. Xu, L. Yang, X. Wei, J. Ding, J. Zhong, P.K. Chu, *Adv. Funct. Mater.* **26** (2016) 3349–3358.
- [99] H. Song, K.T. Lee, M.G. Kim, L.F. Nazar, J. Cho, *Adv. Funct. Mater.* **20** (2010) 3818–3834.
- [100] M. Balogun, Y. Zhu, W. Qiu, Y. Luo, Y. Huang, C. Liang, X. Lu, Y. Tong, *ACS Appl. Mater. Interfaces* **7** (2015) 25991–26003.
- [101] C. Huang, S. Zhao, H. Peng, Y. Lin, C. Nan, G. Cao, *J. Mater. Chem. 6* (2018) 14339–14351.
- [102] H. Wang, L. Wang, J. Lin, J. Yang, F. Wu, L. Li, R. Chen, *Electrochim. Acta* **368** (2021), 137470.
- [103] L. Tang, Y. He, C. Wang, S. Wang, M. Wagemaker, B. Li, Q. Yang, F. Kang, *Adv. Sci.* **4** (2017), 1600311.
- [104] D. Wang, H. Liu, M. Li, X. Wang, S. Bai, Y. Shi, J. Tian, Z. Shan, Y.S. Meng, P. Liu, Z. Chen, *Energy Storage Mater.* **21** (2019) 361–371.
- [105] W.U. Rehman, H. Wang, R.Z.A. Manj, W. Luo, J. Yang, *Small* **17** (2021), 1904508.
- [106] J. Guo, D. Dong, J. Wang, D. Liu, X. Yu, Y. Zheng, Z. Wen, W. Lei, Y. Deng, J. Wang, G. Hong, H. Shao, *Adv. Funct. Mater.* **31** (2021), 2102546.
- [107] P. Li, G. Zhao, X. Zheng, X. Xu, C. Yao, W. Sun, S.X. Dou, *Energy Storage Mater.* **15** (2018) 422–446.
- [108] G. Zhu, D. Chao, W. Xu, M. Wu, H. Zhang, *ACS Nano* **15** (2021) 15567–15593.
- [109] J. Wu, F. Ma, X. Liu, X. Fan, L. Shen, Z. Wu, X. Ding, X. Han, Y. Deng, W. Hu, C. Zhong, *Small Methods* **3** (2019), 1900158.
- [110] S. Chae, M. Ko, K. Kim, K. Ahn, J. Cho, *Joule* **1** (2017) 47–60.
- [111] G. Huang, J. Han, Z. Lu, D. Wei, H. Kashani, K. Watanabe, M. Chen, *ACS Nano* **14** (2020) 4374–4382.
- [112] B. Liang, Y. Liu, Y. Xu, *J. Power Sources* **267** (2014) 469–490.
- [113] K. Feng, M. Li, W. Liu, A.G. Kashkooli, X. Xiao, M. Cai, Z. Chen, *Small* **14** (2018), 1702737.
- [114] B. Wang, J. Ryu, S. Choi, X. Zhang, D. Pribat, X. Li, L. Zhi, S. Park, R.S. Ruoff, *ACS Nano* (2019) 2307–2315.
- [115] M. Liu, H. Gao, G. Hu, K. Zhu, H. Huang, *J. Energy Chem.* **40** (2020) 89–98.
- [116] M. Ko, S. Chae, J. Ma, N. Kim, H. Lee, Y. Cui, J. Cho, *Nat. Energy* **1** (2016).
- [117] N. Liu, J. Liu, D. Jia, Y. Huang, J. Luo, X. Mamad, Y. Yu, Y. Dong, G. Hu, *Energy Storage Mater.* **18** (2019) 165–173.
- [118] H. Mi, X. Yang, Y. Li, P. Zhang, L. Sun, *Chem. Eng. J.* **351** (2018) 103–109.
- [119] H. Li, H. Li, Y. Lai, Z. Yang, Q. Yang, Y. Liu, Z. Zheng, Y. Liu, Y. Sun, B. Zhong, Z. Wu, X. Guo, *Adv. Energy Mater.* **12** (2022), 2102181.
- [120] W. An, P. He, Z. Che, C. Xiao, E. Guo, C. Pang, X. He, J. Ren, G. Yuan, N. Du, D. Yang, D. Peng, Q. Zhang, *ACS Appl. Mater. Interfaces* **14** (2022) 10308–10318.
- [121] T. Ruan, S. Lu, J. Lu, J. Niu, R. Li, *Energy Storage Mater.* **55** (2023) 546–555.
- [122] B. Cao, Y. Li, M. Zhang, N. Cheng, M. Shen, B. Hu, J. Li, Z. Li, S. Xu, W. Zhao, N. Yang, J. Sun, S. Dou, Y. Ren, H. Chen, L. Yin, F. Pan, *J. Power Sources* **551** (2022), 232148.
- [123] J. Wang, X. Sun, *Energy Environ. Sci.* **8** (2015) 1110–1138.
- [124] Y. Wang, P. He, H. Zhou, *Energy Environ. Sci.* **4** (2011) 805–817.
- [125] X. Yang, T. Liu, C. Wang, *Nat. Energy* **6** (2021) 176–185.
- [126] S. Nishimura, G. Kobayashi, K. Ohoyama, R. Kanno, M. Yashima, A. Yamada, *Nat. Mater.* **7** (2008) 707–711.
- [127] B. Kang, G. Ceder, *Nature* **458** (2009) 190–193.
- [128] Y. Zheng, Y. He, K. Qian, B. Li, X. Wang, J. Li, S.W. Chiang, C. Miao, F. Kang, J. Zhang, *Electrochim. Acta* **176** (2015) 270–279.
- [129] Y. Zhang, Q. Huo, P. Du, L. Wang, A. Zhang, Y. Song, Y. Lv, G. Li, *Synthetic Met* **162** (2012) 1315–1326.
- [130] Z. Wang, Y. Lu, *ACS Appl. Mater. Interfaces* **11** (2019) 13225–13233.
- [131] L. Li, L. Wu, F. Wu, S. Song, X. Zhang, C. Fu, D. Yuan, Y. Xiang, *J. Electrochem. Soc.* **164** (2017) A2138–A2150.
- [132] X. Wang, Z. Feng, J. Huang, W. Deng, X. Li, H. Zhang, Z. Wen, *Carbon* **127** (2018) 149–157.
- [133] A. Eftekhari, *J. Power Sources* **343** (2017) 395–411.
- [134] G. Longoni, J.K. Panda, L. Gagliani, R. Brescia, L. Manna, F. Bonaccorso, V. Pellegrini, *Nano Energy* **51** (2018) 656–667.
- [135] Y. Liu, J. Wang, J. Liu, M.N. Banis, B. Xiao, A. Lushington, W. Xiao, R. Li, T. Sham, G. Liang, X. Sun, *Nano Energy* **45** (2018) 52–60.
- [136] M. Shi, R. Li, Y. Liu, J. Liu, *J. Alloys Compd.* **854** (2021), 157162.
- [137] H. Kim, G. Bae, S. Lee, J. Ahn, J. Kim, *Electrochim. Acta* **300** (2019) 18–25.
- [138] L. Gao, Z. Xu, S. Zhang, *J. Alloys Compd.* **739** (2018) 529–535.
- [139] S. Deng, H. Wang, H. Liu, J. Liu, H. Yan, *Nano-Micro Lett.* **6** (2014).
- [140] T. Yoshinari, K. Yamamoto, M. Nishijima, K. Fukuda, A. Kuwabara, I. Tanaka, K. Maeda, H. Kageyama, Y. Orikasa, Y. Uchimoto, *ACS Appl. Energy Mater.* **1** (2018) 6736–6740.
- [141] Y. Chiang, S. Chung, J.T. Bloking, *Nat. Mater.* **1** (2002) 123–128.
- [142] M. Wagemaker, B.L. Ellis, D. Lützenkirchen-Hecht, F.M. Mulder, L.F. Nazar, *Chem. Mater.* **20** (2008) 6313–6315.
- [143] H. Zhang, *Int. J. Electrochim. Sci.* (2020) 12041–12067.
- [144] Y. Zhang, J.A. Alarco, J.Y. Nerkar, A.S. Best, G.A. Snook, P.C. Talbot, B.C. Cowie, *ACS Appl. Energy Mater.* **3** (2020) 9158–9167.
- [145] A. Zhang, *Int. J. Electrochim. Sci.* (2018) 5243–5252.
- [146] P. Liu, Y. Zhang, P. Dong, Y. Zhang, Q. Meng, S. Zhou, X. Yang, M. Zhang, X. Yang, *J. Alloys Compd.* **860** (2021), 157909.
- [147] D. Goonetilleke, T. Faulkner, V.K. Peterson, N. Sharma, *J. Power Sources* **394** (2018) 1–8.
- [148] Z. Xu, L. Gao, Y. Liu, L. Li, *J. Electrochim. Soc.* **163** (2016) A2600–A2610.
- [149] Y. Li, Y. Zhang, J. Ma, L. Yang, X. Li, E. Zhao, S. Fan, G. Xu, S. Yang, C. Yang, *J. Electrochim. Soc.* **166** (2019) A410–A415.
- [150] C. Yan, K. Wu, P. Jing, H. Luo, Y. Zhang, *Mater. Chem. Phys.* **280** (2022), 125711.
- [151] K. Okada, I. Kimura, K. Machida, *RSC Adv.* **8** (2018) 5848–5853.
- [152] H. Liu, S. Luo, S. Yan, Y. Wang, Q. Wang, M. Li, Y. Zhang, *J. Electroanal. Chem.* **850** (2019), 113434.
- [153] M.K. Devaraju, I. Honma, *Adv. Energy Mater.* **2** (2012) 284–297.
- [154] Z. Li, J. Yang, T. Guang, B. Fan, K. Zhu, X. Wang, *Small Methods* **5** (2021), 2100193.
- [155] M.A.M.M. Alsamet, E. Burgaz, *Electrochim. Acta* **367** (2021), 137530.
- [156] C. Yang, D.J. Lee, H. Kim, K. Kim, J. Joo, W.B. Kim, Y.B. Song, Y.S. Jung, J. Park, *RSC Adv.* **9** (2019) 13714–13721.
- [157] S. Zhou, T. Mei, X. Wang, Y. Qian, *Nanoscale* **10** (2018) 17435–17455.
- [158] B. Pei, H. Yao, W. Zhang, Z. Yang, *J. Power Sources* **220** (2012) 317–323.

- [159] J.B. Goodenough, K. Mizushima, T. Takeda, *Jpn. J. Appl. Phys.* 19 (1980) 305.
- [160] T. Ohzuku, A. Ueda, *J. Electrochem. Soc.* 141 (1994) 2972–2977.
- [161] H. Gabrisch, R. Yazami, B. Fultz, *J. Electrochem. Soc.* 151 (2004) A891–A897.
- [162] H. Tukamoto, A.R. West, *J. Electrochem. Soc.* 144 (1997) 3164.
- [163] M. Shibuya, T. Nishina, T. Matsue, I. Uchida, *J. Electrochem. Soc.* 143 (1996).
- [164] S.D. Zhang, M.Y. Qi, S.J. Guo, Y.G. Sun, X.X. Tan, P.Z. Ma, J.Y. Li, R.Z. Yuan, A. M. Cao, L.J. Wan, *Small Methods* 6 (2022), 2200148.
- [165] Z. Chen, J.R. Dahn, *Electrochim. Acta* 49 (2004) 1079–1090.
- [166] K. Wang, J. Wan, Y. Xiang, J. Zhu, Q. Leng, M. Wang, L. Xu, Y. Yang, *J. Power Sources* 460 (2020), 228062.
- [167] M. Yoon, Y. Dong, Y. Yeo, S. Myeong, J. Hwang, J. Kim, S.H. Choi, J. Sung, S. J. Kang, J. Li, J. Cho, *Adv. Funct. Mater.* 30 (2020), 1907903.
- [168] Y. Lyu, X. Wu, K. Wang, Z. Feng, T. Cheng, Y. Liu, M. Wang, R. Chen, L. Xu, J. Zhou, Y. Lu, B. Guo, *Adv. Energy Mater.* 11 (2021), 2000982.
- [169] Y. Huang, Y. Zhu, H. Fu, M. Ou, C. Hu, S. Yu, Z. Hu, C.T. Chen, G. Jiang, H. Gu, H. Lin, W. Luo, Y. Huang, *Angew. Chem. Int. Ed.* 60 (2021) 4682–4688.
- [170] G. Ceder, Y.M. Chiang, D.R. Sadoway, M.K. Aydinol, Y.I. Jang, B. Huang, *Nature* 392 (1998) 694–696.
- [171] Y. Deng, T. Kang, Z. Ma, X. Tan, X. Song, Z. Wang, P. Pang, D. Shu, X. Zuo, J. Nan, *Electrochim. Acta* 295 (2019) 703–709.
- [172] Y. Yu, W. Kong, W. Yang, J. Yang, Y. Chai, X. Liu, *J. Phys. Chem. C* 125 (2021) 2364–2372.
- [173] S. Mou, K. Huang, M. Guan, X. Ma, J.S. Chen, Y. Xiang, X. Zhang, *J. Power Sources* 505 (2021), 230067.
- [174] J. Zhang, Q. Li, C. Ouyang, X. Yu, M. Ge, X. Huang, E. Hu, C. Ma, S. Li, R. Xiao, W. Yang, Y. Chu, Y. Liu, H. Yu, X. Yang, X. Huang, L. Chen, H. Li, *Nat. Energy* 4 (2019) 594–603.
- [175] J. Hu, F. Fan, Q. Zhang, S. Zhong, Q. Ma, *J. Energy Chem.* 67 (2022) 604–612.
- [176] C. Zhang, W. Jiang, W. He, W. Wei, *Energy Storage Mater.* 37 (2021) 161–189.
- [177] X. Hu, W. Yang, Z. Jiang, Z. Huang, Y. Wang, S. Wang, *Electrochim. Acta* 380 (2021), 138227.
- [178] B. Shen, X. Xu, W. Liu, M. Qin, W. Wang, *ACS Appl. Energy Mater.* 4 (2021) 12917–12926.
- [179] T. Fan, W. Kai, V.K. Harika, C. Liu, A. Nimkar, N. Leifer, S. Maiti, J. Grinblat, M. N. Tsibary, X. Liu, M. Wang, L. Xu, Y. Lu, Y. Min, N. Shpigel, D. Aurbach, *Adv. Funct. Mater.* (2022), 2204972.
- [180] T. Cheng, Z. Ma, R. Qian, Y. Wang, Q. Cheng, Y. Lyu, A. Nie, B. Guo, *Adv. Funct. Mater.* 31 (2021), 2001974.
- [181] G. Lu, W. Peng, Y. Zhang, X. Wang, X. Shi, D. Song, H. Zhang, L. Zhang, *Electrochim. Acta* 368 (2021), 137639.
- [182] A. Zhou, Q. Liu, Y. Wang, W. Wang, X. Yao, W. Hu, L. Zhang, X. Yu, J. Li, H. Li, *J. Mater. Chem. C* 5 (2017) 24361–24370.
- [183] B. Hu, F. Geng, M. Shen, C. Zhao, Q. Qiu, Y. Lin, C. Chen, W. Wen, S. Zheng, X. Hu, C. Li, B. Hu, *J. Power Sources* 516 (2021), 230661.
- [184] L. Liu, M. Li, L. Chu, B. Jiang, R. Lin, X. Zhu, G. Cao, *Prog. Mater. Sci.* 111 (2020), 100655.
- [185] C. Xu, P.J. Reeves, Q. Jacquet, C.P. Grey, *Adv. Energy Mater.* 11 (2021), 2003404.
- [186] S.S. Zhang, *Energy Storage Mater.* 24 (2020) 247–254.
- [187] Z. Yang, H. Charalamou, Y. Lin, S.E. Trask, L. Yu, J. Wen, A. Jansen, Y. Tsai, K. M. Wiaderek, Y. Ren, I. Bloom, *J. Power Sources* 521 (2022), 230961.
- [188] G.L. Xu, X. Liu, A. Daali, R. Amine, Z. Chen, K. Amine, *Adv. Funct. Mater.* 30 (2020), 2004748.
- [189] Q. Xie, W. Li, A. Manthiram, *Chem. Mater.* 31 (2019) 938–946.
- [190] Y. Zhang, H. Li, J. Liu, J. Zhang, F. Cheng, J. Chen, *J. Mater. Chem. C* 7 (2019) 20958–20964.
- [191] A. Gomez Martin, F. Reissig, L. Frankenstein, M. Heidbüchel, M. Winter, T. Placke, R. Schmuck, *Adv. Energy Mater.* (2022), 2103045.
- [192] F. Wu, N. Liu, L. Chen, N. Li, Y. Lu, D. Cao, M. Xu, Z. Wang, Y. Su, *ACS Appl. Mater. Interfaces* 13 (2021) 24925–24936.
- [193] J. Yang, Y. Chen, Y. Li, X. Xi, J. Zheng, Y. Zhu, Y. Xiong, S. Liu, *ACS Appl. Mater. Interfaces* 13 (2021) 25981–25992.
- [194] C. Choi, J. Park, Y. Sun, C.S. Yoon, *J. Power Sources* 513 (2021), 230548.
- [195] L. Zhao, G. Chen, Y. Weng, T. Yan, L. Shi, Z. An, D. Zhang, *Chem. Eng. J.* 401 (2020), 126138.
- [196] T. Liu, L. Yu, J. Lu, T. Zhou, X. Huang, Z. Cai, A. Dai, J. Gim, Y. Ren, X. Xiao, M. V. Holt, Y.S. Chu, I. Arslan, J. Wen, K. Amine, *Nat. Commun.* 12 (2021).
- [197] J. Kim, X. Zhang, J. Zhang, A. Manthiram, Y.S. Meng, W. Xu, *Mater. Today* (2021) 155–182.
- [198] J. Wang, H. Kim, H. Hyun, S. Jo, J. Han, D. Ko, S. Seo, J. Kim, H. Kong, J. Lim, *Small Methods* 4 (2020), 2000551.
- [199] S. Zhang, J. Ma, Z. Hu, G. Cui, L. Chen, *Chem. Mater.* 31 (2019) 6033–6065.
- [200] X. Fan, X. Ou, W. Zhao, Y. Liu, B. Zhang, J. Zhang, L. Zou, L. Seidl, Y. Li, G. Hu, C. Battaglia, Y. Yang, *Nat. Commun.* 12 (2021) 5230.
- [201] S. Wang, A. Dai, Y. Cao, H. Yang, A. Khalil, J. Lu, H. Li, X. Ai, *J. Mater. Chem. 9* (2021) 11623–11631.
- [202] P. Yan, J. Zheng, J. Liu, B. Wang, X. Cheng, Y. Zhang, X. Sun, C. Wang, J. Zhang, *Nat. Energy* 3 (2018) 600–605.
- [203] H.H. Sun, A. Dolocan, J.A. Weeks, A. Heller, C.B. Mullins, *ACS Nano* 14 (2020) 17142–17150.
- [204] X. Xu, H. Huo, J. Jian, L. Wang, H. Zhu, S. Xu, X. He, G. Yin, C. Du, X. Sun, *Adv. Energy Mater.* 9 (2019), 1803963.
- [205] K. Xu, *Chem. Rev.* 114 (2014) 11503–11618.
- [206] K. Xu, *Chem. Rev.* 104 (2004) 4303–4418.
- [207] M. Xia, T. Jiao, G. Liu, Y. Chen, J. Gao, Y. Cheng, Y. Yang, M. Wang, J. Zheng, *J. Power Sources* 548 (2022), 232106.
- [208] N. Gao, S. Kim, P. Chinnam, E.J. Dufek, A.M. Colclasure, A. Jansen, S. Son, I. Bloom, A. Dunlop, S. Trask, K.L. Gering, *Energy Storage Mater.* 44 (2022) 296–312.
- [209] L.L. Jiang, C. Yan, Y.X. Yao, W. Cai, J.Q. Huang, Q. Zhang, *Angew. Chem. Int. Ed.* 133 (2021) 3444–3448.
- [210] Y.X. Yao, X. Chen, C. Yan, X.Q. Zhang, W.L. Cai, J.Q. Huang, Q. Zhang, *Angew. Chem. Int. Ed.* 133 (2021) 4136–4143.
- [211] E.R. Logan, D.S. Hall, M.M.E. Cormier, T. Taskovic, M. Bauer, J. Hamam, H. Hebecker, L. Molino, J.R. Dahn, *J. Phys. Chem. C* 124 (2020) 12269–12280.
- [212] X. Fan, X. Ji, L. Chen, J. Chen, T. Deng, F. Han, J. Yue, N. Piao, R. Wang, X. Zhou, X. Xiao, L. Chen, C. Wang, *Nat. Energy* 4 (2019) 882–890.
- [213] X. Ma, R.S. Arumugam, L. Ma, E. Logan, E. Tonita, J. Xia, R. Petibon, S. Kohn, J. R. Dahn, *J. Electrochem. Soc.* 164 (2017) A3556–A3562.
- [214] S.H. Lee, J.Y. Hwang, J. Ming, Z. Cao, H.A. Nguyen, H.G. Jung, J. Kim, Y.K. Sun, *Adv. Energy Mater.* 10 (2020), 2000567.
- [215] C.V. Amanchukwu, X. Kong, J. Qin, Y. Cui, Z. Bao, *Adv. Energy Mater.* 9 (2019), 1902116.
- [216] J. Chen, H. Lu, X. Zhang, Y. Zhang, J. Yang, Y. Nuli, Y. Huang, J. Wang, *Energy Storage Mater.* 50 (2022) 387–394.
- [217] Y.X. Yao, X. Chen, N. Yao, J.H. Gao, G. Xu, J.F. Ding, C.L. Song, W.L. Cai, C. Yan, Q. Zhang, *Angew. Chem. Int. Ed.* 135 (2023), 202214828.
- [218] Y. Yang, Z. Fang, Y. Yin, Y. Cao, Y. Wang, X. Dong, Y. Xia, *Angew. Chem. Int. Ed.* 134 (2022).
- [219] H. Liang, Z. Gu, X. Zhao, J. Guo, J. Yang, W. Li, B. Li, Z. Liu, Z. Sun, J. Zhang, X. Wu, *Sci. Bull.* 67 (2022) 1581–1588.
- [220] S. Qi, J. Liu, J. He, H. Wang, M. Wu, D. Wu, J. Huang, F. Li, X. Li, Y. Ren, J. Ma, *J. Energy Chem.* 63 (2021) 270–277.
- [221] H.Q. Pham, M.T. Nguyen, M. Tarik, M. El Kazzi, S. Trabesinger, *ChemSusChem* 14 (2021) 2461–2474.
- [222] C. Wölke, D. Diddens, B. Heidrich, M. Winter, I. Cekic Laskovic, *Chemelectrochem* 8 (2021) 972–982.
- [223] N. Yeh, F. Wang, C. Khotimah, X. Wang, Y. Lin, S. Chang, C. Hsu, Y. Chang, L. Tiong, C. Liu, Y. Lu, Y. Liao, C. Chang, S. Haw, C. Pao, J. Chen, C. Chen, J. Lee, T. Chan, H. Sheu, J. Chen, A. Ramar, C. Su, *ACS Appl. Mater. Interfaces* 13 (2021) 7355–7369.
- [224] Z. Xiao, S. Cui, Y. Wang, S. Liu, G. Li, X. Gao, *ACS Sustain. Chem. Eng.* (2021) 1958–1968.
- [225] Z. Chen, W.Q. Lu, J. Liu, K. Amine, *Electrochim. Acta* 51 (2006) 3322–3326.
- [226] D.Y. Wang, A. Xiao, L. Wells, J.R. Dahn, *J. Electrochem. Soc.* 162 (2014) A169–A175.
- [227] S. Zhang, G. Yang, Z. Liu, X. Li, X. Wang, R. Chen, F. Wu, Z. Wang, L. Chen, *Nano Lett.* 21 (2021) 3310–3317.
- [228] Y. Yang, H. Zhou, J. Xie, L. Bao, T. Li, J. Lei, J. Wang, *J. Energy Chem.* 66 (2022) 647–656.
- [229] W. Xiao, H. Xu, M. Xuan, Z. Wu, Y. Zhang, X. Zhang, S. Zhang, Y. Shen, G. Shao, *J. Energy Chem.* 53 (2021) 147–154.
- [230] Y. Zou, Z. Ma, G. Liu, Q. Li, D. Yin, X. Shi, Z. Cao, Z. Tian, H. Kim, Y. Guo, C. Sun, L. Cavallo, L. Wang, H.N. Alshareef, Y.K. Sun, J. Ming, *Angew. Chem. Int. Ed.* 135 (2023), 202216189.